Self-similarity in quantum dynamics

L. E. Reichl and Li Haoming*
Center for Statistical Mechanics, University of Texas at Austin, Austin, Texas 78712
(Received 16 February 1990)

We have developed a renormalization transformation, based on the existence of higher-order nonlinear resonances in the double-resonance model, that gives good predictions for the extension of the wave function in that system due to nonlinear resonance overlap. The double-resonance model describes the qualitative behavior, in local regions of the Hilbert space, of many quantum systems with two degrees of freedom whose dynamics is described by a nonlinear Hamiltonian but a linear Schrödinger equation.

I. INTRODUCTION

The phase space of nonlinear nonintegrable classical conservative systems exhibits extremely complex structure consisting of regular Kolmogorov-Arnold-Moser (KAM) tori intermixed with chaos. In some regions of the phase space the structure is self-similar to all length scales and exhibits scaling behavior in space and time. KAM tori are the remnants of global conserved quantities. For many systems, when some parameter which characterizes the size of the nonlinearity is small, KAM tori dominate the phase space. However, as the nonlinearity parameter is increased in size, nonlinear resonances in the system grow and overlap and destroy KAM tori lying between them. The existence of KAM tori can have a profound effect on the dynamics of a conservative system with two degrees of freedom because some KAM tori can divide the phase space into disjoint parts. When such a KAM torus is destroyed by nonlinear resonance overlap, the dynamics of the classical system may change dramatically.

The mechanism by which KAM surfaces are destroyed by nonlinear resonances has been studied extensively by Greene,[1] Shenker and Kadanoff,[2] MacKay,[3] and others. KAM tori have irrational winding numbers. Each irrational winding number can be represented uniquely by a continued fraction. Greene showed that associated with this continued fraction is a unique infinite sequence of nonlinear resonances which approximate the KAM torus. If the winding number of the KAM torus is represented by the continued fraction

$$w \equiv [a_0, a_1, a_2, \ldots] = a_0 + \cfrac{1}{a_1 + \cfrac{1}{a_2 + \cdots}} ,$$

then the resonances which approximate the KAM torus have periodic orbits with winding numbers

$$w_n \equiv [a_0, a_1, a_2, \ldots, a_n, \infty]$$

with $\lim_{n\to\infty} w_n = w$. The resonances having periodic orbits with winding numbers w_0, w_1, w_2, etc. alternatively lie on opposite sides of the KAM torus. The width of each resonance depends on the nonlinearity parameter of the system. As this parameter is increased, resonances on an ever smaller scale grow until at a critical value of the nonlinearity parameter, all resonances in the sequence have grown large enough to punch holes in the KAM torus making it a Cantorus, a barrier with a Cantor set of holes through which phase-space trajectories can leak. The KAM torus breaks abruptly as a function of the nonlinearity parameter. As the nonlinearity parameter increases further, the Cantorus gradually disappears.

The behavior of nonlinear resonances is easiest to study in nonlinear systems which are driven by a periodic external field. Because of the nonlinearity of the driven system, the external field induces infinite sets of nonlinear resonances in the phase space of the system. When the Hamiltonian is written in terms of the action-angle variables of the driven system, the induced resonances appear as traveling potential-energy waves in the phase space (cf. Appendixes A and B for examples). These are called the primary resonances of the system. The primary resonances interact to produce infinite families of higher-order resonances. There is considerable numerical evidence that the behavior of the phase space between any two primary resonances is largely determined by those two primary resonances and that the effects of primary resonances outside this region tend to average out. Therefore, in order to analyze the mechanism for destruction of KAM tori between two given primary resonances, it is often sufficient to consider a Hamiltonian composed of only those two resonances. It is this fact that underlies the renormalization procedure of Escande and Doveil.[4,5] They begin with a Hamiltonian which describes a system with two primary resonances. It consists of a particle moving in the presence of two cosine potential-energy waves, one of which is at rest and another which is traveling through phase space. This Hamiltonian, which they call the paradigm Hamiltonian, depends on only three parameters, the amplitudes of the two cosine waves and the relative wave number of the two waves. The renormalization proceeds as follows. They focus on a given KAM torus between the two primary resonances. By a sequence of canonical transformations they can select the two daughter resonances which bracket this KAM surface. They then write a paradigm Hamiltonian for these daughter resonances and neglect

contributions coming from all other daughter resonances. In so doing they obtain a new paradigm Hamiltonian with two primary resonances and new amplitudes and wave number. By repeating the process they obtain a mapping of the amplitudes and wave number to ever smaller scales in the phase space. The properties of this map can be used to determine whether or not various KAM tori exist for a given initial paradigm Hamiltonian.

There is now considerable evidence that nonlinear resonances and KAM-like behavior exist in quantum-mechanical systems. Geisel, Radons, and Rubner[6] have studied the effect of KAM tori and Cantori, which are known to be present in the classical standard map, on the spread of probability in the quantum standard map. They find that KAM tori and Cantori act as barriers to the spread of probability and that probability decays exponentially across these barriers. Brown and Wyatt[7] have shown that a similar type of behavior exists for a driven oscillator model. The phenomenon of nonlinear resonance and resonance overlap in quantum dynamics has been studied extensively by Berman, Zaslavsky, and Kolovsky,[8] Lin and Reichl,[9,10] and Toda and Ikeda.[11] We now know that just as for classical systems, nonlinear resonance regions exist in the Hilbert space and for a small nonlinearity parameter remain isolated from one another. However, as the nonlinearity parameter is increased resonances can overlap leading to an extension of the wave function in the region of the influence of the overlapping resonances. In addition, resonance overlap leads to a change in the spectral statistics of states involved in the resonance overlap,[10] from a Poisson-like to a Wigner-like distribution. This is considered one of the manifestations of chaos in quantum systems. Recently, Reichl[12] has given numerical evidence that primary nonlinear resonances in Hilbert space generate higher-order resonances and that these play a role in facilitating resonance overlap in quantum systems just as they do in classical systems.

In this paper we shall show that renormalization techniques analogous to those of Escande and Doveil can be developed to describe the phenomenon of resonance overlap and extension of the wave function in quantum systems just as it can be for a classical system. However, rather than perform the renormalization on the Hamiltonian as is done classically, we shall perform the renormalization directly on the Schrödinger equation. We shall begin with a general double-resonance model which consists of two traveling cosine potential waves (two primary resonances). The renormalization procedure requires that the amplitude of one of the waves be larger than the other so that wave will dominate the system. We then rewrite the Schrödinger equation in terms of eigenstates of the system consisting of only a single large wave (this is an integrable system). By so doing, we come close to solving the problem. However, we find that in this new basis, the Schrödinger equation contains an infinite number of higher-order (daughter) resonances. We then focus on a given pair of daughters and write a double-resonance Schrödinger equation for them. This procedure can be repeated and gives a renormalization mapping which enables us to determine parameters of the initial double-resonance model for which overlap occurs. Our results give much better estimates for resonance overlap than does the simple Chirikov estimate used until now for quantum systems.

We shall begin in Sec. II by writing a general double-resonance Schrödinger equation and then we will transform it into the form of a paradigm Schrödinger equation which is the basis of our renormalization transformation. In Sec III we obtain WKB solutions for energies and eigenstates of the single-resonance Schrödinger equation in the region outside the resonance and we show that the WKB energies agree fairly well with exact energies obtained numerically. These analytic expressions enable us to build the renormalization transformation. In Sec. IV we use the WKB solutions to write the double-resonance Schrödinger equation in terms of eigenstates of the single-resonance equation. This generates an infinite family of higher resonances. We show that the WKB amplitudes for the higher-order resonances agree fairly well with exact numerical expressions.

In Sec. V we write the renormalization mapping for this system. The renormalization map relates the relative wave number and amplitudes of a resonance pair at one level (scale) to those at a higher level (smaller scale). The renormalization mapping thus allows us to examine a sequence of resonance pairs on an ever smaller scale in the Hilbert space. Bounded quantum systems have a discrete spectrum so that in actuality we cannot go to infinitely small scale in such systems. However, the mappings have a stable manifold which separates regions in which resonance overlap at smaller scale does not occur (the stable side) from regions in which it does occur (the unstable side). In the unstable region, the amplitudes grow so rapidly as we go to small scale that the mapping still gives good predictions.

In Sec. VI we give numerical results showing that steps by which overlap of the two primary resonances occurs and we compare the renormalization predictions with observed results. Finally, in Sec. VII we make some concluding remarks.

II. THE PARADIGM SCHRÖDINGER EQUATION

The manifestations of chaos occur in quantum systems when nonlinear quantum resonances zones overlap in the unperturbed Hilbert space.[10] As we have shown in Ref. 12, resonance overlap is facilitated by the existence of higher-order nonlinear resonances that are generated by the interaction of primary resonances. In this paper we explore the structure of the network of nonlinear resonances generated by any given pair of primary resonances and develop a renormalization scheme to describe the overlap of any given sequence of successively higher-order resonance pairs.

Let us consider a typical pair of resonances found in the standard map or square-well system discussed in Appendixes A and B. The Schrödinger equation can be written

$$-i\frac{\partial\langle\theta|\Psi^{(0)}(t)\rangle}{\partial t}=-\frac{\partial^2\langle\theta|\Psi^{(0)}(t)\rangle}{\partial\theta^2}+\{V_a(0)\cos[\mu_a(0)\theta-\omega_0 t]+V_b(0)\cos[\mu_b(0)\theta\pm\omega_0 t]\}\times\langle\theta|\Psi^{(0)}(t)\rangle \tag{2.1}$$

where $V_a(0)$ and $V_b(0)$ are the amplitudes of the cosine waves, $\mu_a(0)$ and $\mu_b(0)$ are wave numbers of the cosine waves, ω_0 is a radial frequency associated with this time periodic system, and $|\Psi^{(0)}\rangle$ is the state of the system. The parameters $V_i(0)$ and ω_0 depend on Planck's constant $\hbar$ as $V_i(0)\sim\hbar^{-2}$ and $\omega_0\sim\hbar^{-1}$. The index 0 on the above quantities indicates that we are at the zeroth level of the renormalization transformation. We shall assume that our system has periodic boundary conditions with period $2\pi N$ and therefore we require that $\langle\theta|\Psi^{(0)}(t)\rangle=\langle\theta+2\pi N|\Psi^{(0)}(t)\rangle$ and that $\mu_i(0)=M_i(0)/N$ $(i=a,b)$, where $M_i(0)$ are integers. We can also write Eq. (2.1) in terms of a traveling-wave basis. If we note that

$$\langle\theta|\Psi^{(0)}(t)\rangle=\sum_{k=-\infty}^{\infty}e^{ik\theta}\langle k|\Psi^{(0)}(t)\rangle\ , \tag{2.2}$$

where k is a rational fraction, $k=n/N$, n is an integer, and the summation $\sum_{k=-\infty}^{\infty}$ is over all values in k. In terms of the states $\langle k|\Psi^{(0)}(t)\rangle$ Eq. (2.1) takes the form

$$-i\frac{\partial\langle k|\Psi^{(0)}(t)\rangle}{\partial t}=k^2\langle k|\Psi^{(0)}(t)\rangle+\frac{V_a(0)}{2}[e^{-i\omega_0 t}\langle k-\mu_a(0)|\Psi^{(0)}(t)\rangle+e^{i\omega_0 t}\langle k+\mu_a(0)|\Psi^{(0)}(t)\rangle]+\frac{V_b(0)}{2}[e^{\pm i\omega_0 t}\langle k-\mu_b(0)|\Psi^{(0)}(t)\rangle+e^{\mp i\omega_0 t}\langle k+\mu_b(0)|\Psi^{(0)}(t)\rangle]\ . \tag{2.3}$$

As we have shown in Refs. 9 and 12, the resonance due to cosine wave $\cos[\mu_i(0)\theta\pm\omega_0 t]$ occurs at $k=\bar{k}_i=\mp\omega_0/2\mu_i(0)$ where $i=a,b$, and has a half-width $\Delta k_i=[2V_i(0)]^{1/2}$.

We can transform to the rest frame of the cosine wave $\cos[\mu_a(0)\theta-\omega_0 t]$ via a unitary transformation

$$\hat{U}_{\mu_a(0)}(t)=\exp(-i\hat{P}_{\mu_a(0)}t)\ , \tag{2.4}$$

where

$$\langle k'|\hat{P}_{\mu_a(0)}|k\rangle=(2k\bar{k}_a-\bar{k}_a^{\,2})\delta_{k,k'}\ . \tag{2.5}$$

We introduce a state $|\Phi^{(0)}(t)\rangle$ such that

$$|\Psi^{(0)}(t)\rangle=\hat{U}_{\mu_a(0)}(t)|\Phi^{(0)}(t)\rangle\ . \tag{2.6}$$

The state $|\Phi^{(0)}(t)\rangle$ describes the behavior of the system in the rest frame of the cosine wave, $\cos[\mu_a(0)\theta-\omega_0 t]$. In terms of this state, the Schrödinger equation takes the form

$$-i\frac{\partial\langle k|\Phi^{(0)}(t)\rangle}{\partial t}=(k-\bar{k}_a)^2\langle k|\Phi^{(0)}(t)\rangle+\frac{V_a(0)}{2}[\langle k-\mu_a(0)|\Psi^{(0)}(t)\rangle+\langle k+\mu_a(0)|\Phi^{(0)}(t)\rangle]+\frac{V_b(0)}{2}[e^{+i(\nu_0\pm1)\omega_0 t}\langle k-\mu_b(0)|\Phi^{(0)}(t)\rangle+e^{-i(\nu_0\pm1)\omega_0 t}\langle k+\mu_b(0)|\Phi^{(0)}(t)\rangle] \tag{2.7}$$

where $\nu_0=\mu_b(0)/\mu_a(0)$ is the ratio of the wave numbers of the two cosine waves in Eq. (2.1). If we use the transformation in Eq. (2.2) to transform back to the angle picture, Eq. (2.7) takes the form

$$-i\frac{\partial\langle\theta|\Phi^{(0)}(t)\rangle}{\partial t}=\left[-i\frac{\partial}{\partial\theta}-\bar{k}_a\right]^2\langle\theta|\Phi^{(0)}(t)\rangle+\{V_a(0)\cos[\mu_a(0)\theta]+V_b(0)\cos[\mu_b(0)\theta+(\nu_0\pm1)\omega_0 t]\}\langle\theta|\Phi^{(0)}(t)\rangle\ . \tag{2.8}$$

Let us now rescale the angle so that $\Theta=\mu_a(0)\theta$. Then the stationary cosine oscillates once in period 2π and Eq. (2.8) takes the form

$$-i\frac{\partial\langle\Theta|\Phi^{(0)}(t)\rangle}{\partial t}=\left[-i\mu_a(0)\frac{\partial}{\partial\Theta}-\bar{k}_a\right]^2\langle\Theta|\Phi^{(0)}(t)\rangle+\{V_a(0)\cos(\Theta)+V_b(0)\cos[\nu_0\Theta+(\nu_0\pm1)\omega_0 t]\}\langle\Theta|\Phi^{(0)}(t)\rangle\ . \tag{2.9}$$

If we introduce a change of phase

$$\langle\Theta|\Phi^{(0)}(t)\rangle=\langle\Theta|\chi^{(0)}(t)\rangle e^{i\bar{k}_a\Theta/\mu_a(0)},$$

then Eq. (2.9) takes the form

$$-i\frac{\partial\langle\Theta|\chi^{(0)}(t)\rangle}{\partial t}=-[\mu_a(0)]^2\frac{\partial^2\langle\Theta|\chi^{(0)}(t)\rangle}{\partial\Theta^2}+\{V_a(0)\cos(\Theta)+V_b(0)\cos[\nu_0(\Theta+\bar{\omega}_0 t)]\}\langle\Theta|\chi^{(0)}(t)\rangle \tag{2.10}$$

where $\bar{\omega}_0=[(\nu_0\pm1)/\nu_0]\omega_0$. Equation (2.11) is the paradigm Schrödinger equation and is the starting point of our process of renormalization. In the subsequent sections, we shall always assume that $V_a(0)>V_b(0)$.

III. WKB EXPRESSIONS FOR PENDULUM STATES

In order to obtain an equation for higher-order resonances, we expand Eq. (2.10) in terms of eigenstates of Eq. (2.10) for the case when $V_b(0)=0$. When $V_b(0)=0$, Eq. (2.10) is integrable and is a form of Mathieu equation. If $V_a(0)\gg V_b(0)$ then we come close to solving Eq. (2.10) by doing this, or at least we are in a basis which more adequately describes the actual behavior of the system. However, as we shall see in Sec. IV, we also reveal the fact that this system contains an infinite number of higher-order nonlinear resonances.

Let us consider the quantum pendulum equation (a form of Mathieu equation)

$$E_l\phi_l(\theta)=-\frac{\partial^2\phi_l(\theta)}{\partial\theta^2}+V_a\cos(\mu_a\theta)\phi_l(\theta) \tag{3.1}$$

where $l=m/N\geq0$ (m an integer), $\phi_l(\theta)=\langle\theta|\phi_l\rangle$, and $\phi_l(\theta)$ satisfies the boundary condition $\phi_l(\theta)=\phi_l(\theta+2\pi N)$. Equation (3.1) has solutions of definite parity, $\phi_l^\alpha(\theta)$ ($\alpha=A,S$),

$$E_l^\alpha\phi_l^\alpha(\theta)=-\frac{\partial^2\phi_l^\alpha(\theta)}{\partial\theta^2}+V_a\cos(\mu_a\theta)\phi_l^\alpha(\theta)\ , \tag{3.2}$$

where the symmetric solutions $\phi_l^{(S)}(\theta)$ satisfy the conditions $\phi_l^{(S)}(\theta)=\phi_l^{(S)}(-\theta)$ and $\phi_{-l}^{(S)}(\theta)=\phi_l^{(S)}(\theta)$ and the antisymmetric solutions satisfy the conditions $\phi_l^{(A)}(\theta)=-\phi_l^{(A)}(-\theta)$ and $\phi_{-l}^{(A)}(\theta)=-\phi_l^{(A)}(\theta)$. Furthermore, $E_l^{(\alpha)}$ is an even function of l. In the limit $V_a\to0$, $\phi_l^{(S)}(\theta)\to(1/\sqrt{\pi N})\cos(l\theta)$ and $\phi_l^{(A)}(\theta)\to(i/\sqrt{\pi N})\sin(l\theta)$. Let us now introduce the following functions:

$$\phi_l^{(+)}(\theta)=\frac{1}{\sqrt{2}}[\phi_l^{(S)}(\theta)+\phi_l^{(A)}(\theta)]\ , \tag{3.3a}$$

$$\phi_l^{(-)}(\theta)=\frac{1}{\sqrt{2}}[\phi_l^{(S)}(\theta)-\phi_l^{(A)}(\theta)]\ , \tag{3.3b}$$

for $l>0$ with $\phi_0=\phi_0^{(S)}(\theta)$ and $\phi_0=\phi_0^{(A)}(\theta)=0$. These functions reduce to traveling waves in the limit $V_a\to0$ and have the property that $\phi_{-l}^{(-)}(\theta)=\phi_l^{(+)}(\theta)$. From Eqs. (3.2) and (3.3) we obtain

$$E_p^{(+)}\phi_l^{(+)}(\theta)+E_l^{(-)}\phi_l^{(-)}(\theta)=-\frac{\partial^2\phi_l^{(+)}(\theta)}{\partial\theta^2}+V_a\cos(\mu_a\theta)\phi_l^{(+)}(\theta) \tag{3.4}$$

where $E_l^{(+)}=\frac{1}{2}(E_l^{(+)}+E_l^{(+)})$ and $E_l^{(-)}=\frac{1}{2}(E_l^{(+)}-E_l^{(+)})$. Since $\phi_{-l}^{(-)}(\theta)=\phi_l^{(+)}(\theta)$, we can introduce a new function $\phi_p(\theta)=\phi_{|p|}^{(+)}(\theta)$ and $\phi_{-p}(\theta)=\phi_{|p|}^{(-)}(\theta)$ where p has the range $-\infty\leq p\leq\infty$. Then Eq. (3.4) takes the form

$$E_p^{(+)}\phi_p(\theta)+E_p^{(-)}\phi_{-p}(\theta)=-\frac{\partial^2\phi_p(\theta)}{\partial\theta^2}+V_a\cos(\mu_a\theta)\phi_p(\theta)\ . \tag{3.5}$$

If we make the change of variables, $\Theta=\mu_a\theta$, Eq. (3.5) takes the form

$$E_p^{(+)}\phi_p(\Theta)+E_p^{(-)}\phi_{-p}(\Theta)=-\mu_a^2\frac{\partial^2\phi_p(\Theta)}{\partial\Theta^2}+V_a\cos(\Theta)\phi_p(\Theta)\ . \tag{3.6}$$

Let us now obtain the WKB solutions to these equations. Assume a solution to Eq. (3.1) of the form $\phi_p(\theta)=e^{if_p(\theta)}$. Then

$$if_p''-f_p'^2+[E_p-V_a\cos(\mu_a\theta)]=0\ , \tag{3.7}$$

where $f_p'=df_p/d\theta$. In regions where $|f_p''|\ll1$, the solution to Eq. (3.1) can be written

$$\phi_p(\theta;\mu_a)\approx\psi_p(\theta;\mu_a)=\frac{1}{[\varepsilon_p-V_a\cos(\mu_a\theta)]^{1/4}}\times\exp\left[\frac{i}{\mu_a}\int_0^\theta[\varepsilon_p-V_a\cos(\mu_a\theta)]^{1/2}d\theta\right], \tag{3.8}$$

with $E_p^{(S)}\approx\varepsilon_p$ and $E_p^{(A)}\approx\varepsilon_p$ so that in the WKB approximation $E_p^{(-)}=0$. It is easy to show that the condition of validity, $|f_p''|\ll1$, of the WKB solution implies that the WKB solution will only be valid when $\varepsilon_p\gg U_a$.

The integral appearing in Eq. (3.8) can be done explicitly. We find

$$\int_0^\theta d\theta[\varepsilon_p-V_a\cos(\mu_a\theta)]^{1/2}=\frac{1}{\mu_a}\int_0^{\mu_a\theta}d\Theta[\varepsilon_p-V_a\cos(\Theta)]^{1/2}=\frac{2}{\mu_a}(\varepsilon_p+V_a)^{1/2}[E(\mu_a\theta/2+\pi/2,\kappa)+E(\pi/2,\kappa)]\ , \tag{3.9}$$

where $E(\Theta,\kappa)$ is the incomplete elliptic integral of the second kind, and κ is the modulus and is defined $\kappa^2=2V_a/(\varepsilon_p+V_a)$. The modulus κ in the region of validity of the WKB approximation will be small. Therefore we can expand the right-hand side of Eq. (3.9) in powers of κ. If we keep terms to second order in κ, we obtain

$$\int_0^{\theta} d\theta[\varepsilon_p - V_a\cos(\mu_a\theta)]^{1/2} = \frac{1}{\mu_a}\int_0^{\mu_a\theta} d\Theta[\varepsilon_p - V_a\cos(\Theta)]^{1/2}$$
$$\approx \frac{2}{\mu_a}(\varepsilon_k+V_a)^{1/2}\left[(1-\tfrac{1}{4}\kappa^2)\frac{\mu_a\theta}{2} - \tfrac{1}{8}\kappa^2\sin(\mu_a\theta)\right] . \tag{3.10}$$

The WKB values for the energy eigenvalues ε_p are obtained from the condition

$$\int_0^{2\pi N} d\theta[\varepsilon_p - V_a\cos(\mu_a\theta)]^{1/2} = 2\pi pN \tag{3.11}$$

where p is a rational fraction, $p=m/N$, and m is an integer. Using Eq. (3.6), the quantization condition becomes

$$(\varepsilon_p+V_a)^{1/2}(1-\tfrac{1}{4}\kappa^2)=p . \tag{3.12}$$

Thus the energy is given approximately by

$$\varepsilon_p \approx p^2\left[1-\frac{1}{4}\frac{V_a^2}{p^4}+\frac{1}{4}\frac{V_a^3}{p^6}+\cdots\right] \tag{3.13}$$

and $\varepsilon_p \approx p^2$ when V_a/p^2 is small.

Let us now introduce the quantity

$$x_p = \frac{1}{4\mu_a}\kappa^2(\varepsilon_p+V_a)^{1/2}$$
$$= \frac{V_a}{2\mu_a(\varepsilon_p+V_a)^{1/2}} \approx \frac{V_a}{2p\mu_a}\left[1+\frac{V_a^2}{8p^2\mu_a^2}+\cdots\right] . \tag{3.14}$$

Then the WKB wave function, which is a solution to Eq. (3.1), can be written

$$\psi_p(\theta) \approx \frac{1}{\sqrt{2\pi N}} e^{+i[p\theta - x_p\sin(\mu_a\theta)]} . \tag{3.15}$$

Equation (3.15) is a solution to Eq. (3.1) if we neglect terms of order V_a/p. These will always give contributions of order V_a/p^2 in the subsequent calculations. Equation (3.15) is valid for $p^2 \gg V_a$. The WKB wave function, Eq. (3.15), is normalized to one. A rather lengthy calculation shows that

$$\int_0^{2\pi N} d\theta[\psi_{p'}(\theta)]^*\psi_p(\theta) = \delta_{p'p} . \tag{3.16}$$

The WKB solution to Eq. (3.6) can be written

$$\psi_p(\Theta) \approx \frac{1}{(2\pi M_a)^{1/2}} e^{+i[(p/\mu_a)\Theta - x_p\sin(\Theta)]} \tag{3.17}$$

and satisfies the normalization condition

$$\int_0^{2\pi M_a} d\Theta[\psi_{p'}(\Theta)]^*\psi_p(\Theta) = \delta_{p',p} \tag{3.18}$$

where we have used the fact that $\mu_a N = M_a$. It is useful to note that the WKB wave functions can be expanded in a Fourier series

$$\psi_p(\Theta) = \frac{1}{(2\pi M_a)^{1/2}} \sum_{n=-\infty}^{\infty} J_n(x_p) e^{i(p/\mu_a - n)\Theta} \tag{3.19}$$

where $J_n(x)$ is the Bessel of integer order n.

It is of interest to compare the exact eigenvalues of Eq. (3.2) to the WKB approximation $\varepsilon_p \approx p^2$. In Fig. 1 we plot $E_p^{(+)}$ versus p and compare it to $\varepsilon_p \approx p^2$ for $N=1$ and $M_a=1$ and in a range of values $V_a=240$, 480, 720, 960. In Fig. 2, we plot $E_p^{(-)}$ versus p for the same values of N, M_a, and V_a. We see that $E_p^{(+)} \approx p^2$ when $E_p^{(-)}=0$.

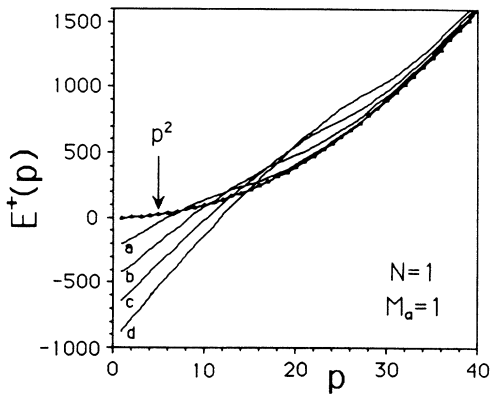

FIG. 1. Plot of $E^{(+)}(p)$ for $N=1$, $M_a=1$. Curves labeled a, b, c, and d correspond to $V_a=240$, 480, 720, and 960, respectively. The four curves were obtained numerically. Also shown is a plot of p^2 vs p. For p large enough, $E_p^{(+)} \approx p^2$.

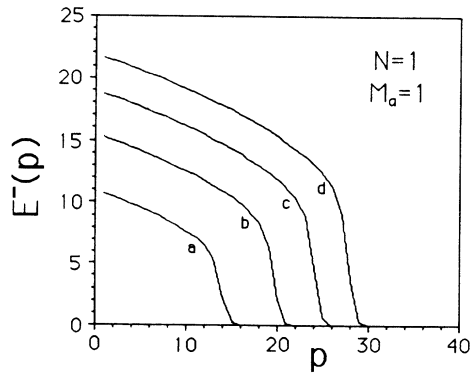

FIG. 2. Plot of $E^{(-)}(p)$ for $N=1$, $M_a=1$. Curves labeled a, b, c, and d correspond to $V_a=240$, 480, 720, and 960, respectively. These curves were obtained numerically.

IV. EXPANSION IN MATHIEU EIGENSTATES

Let us now return to the paradigm Schrödinger equation, Eq. (2.10), and expand it in terms of eigenstates of the Mathieu equation (3.2). We first expand the wave function $\langle\Theta|\chi^{(0)}(t)\rangle$ in a complete set of eigenstates,

$$\langle\Theta|\chi^{(0)}(t)\rangle=\sum_{l=0}^{\infty}[C_l^{(S)}(t)\phi_l^{(S)}(\theta)+C_l^{(A)}(t)\phi_l^{(A)}(\theta)] \tag{4.1}$$

where the functions $\phi_l^{(S)}(\Theta)$ and $\phi_l^{(S)}(\Theta)$ depend on parameters $\mu_a(0)$, N, and $V_a(0)$, and are defined similarly to $\phi_l^{(S)}(\Theta)$ and $\phi_l^{(A)}(\Theta)$. The functions $C_l^{(S)}(t)$ and $C_l^{(A)}(t)$ depend on parameters $\mu_a(0)$, N, ν_0, $\bar{\omega}_0$, $V_a(0)$, and $V_b(0)$. If we substitute Eq. (4.1) into Eq. (2.10) and use the orthonormality of Mathieu eigenstates, we obtain

$$-i\frac{\partial C_l^{(\alpha)}(t)}{\partial t}=E_l^{(\alpha)}C_l^{(\alpha)}(t)+V_b(0)\sum_{l'=0}^{\infty}\int_0^{2\pi M_a}d\Theta[\phi_{l'}^{(\alpha)}(\Theta)]^*\cos[\nu_0(\Theta+\bar{\omega}_0t)]\sum_{\alpha'=S,A}C_l^{(\alpha')}(t)\phi_l^{(\alpha')}(\Theta)\ , \tag{4.2}$$

where $\alpha=S, A$. Let us define

$$C_l^{(+)}=\frac{1}{\sqrt{2}}(C_l^{(S)}+C_l^{(A)}) \text{ and } C_l^{(+)}=\frac{1}{\sqrt{2}}(C_l^{(S)}-C_l^{(A)})\ . \tag{4.3}$$

If we now note that $C_l^{(-)}=C_{-l}^{(+)}$ and combine Eqs. (4.2) and (4.3) we can write (after considerable algebra)

$$-i\frac{\partial C_l^{(+)}(t)}{\partial t}=E_l^{(+)}C_l^{(+)}(t)+E_l^{(-)}C_l^{(-)}(t)$$
$$+\frac{V_b(0)}{\sqrt{2}}\int_0^{2\pi M_a}d\Theta\cos[\nu_0(\Theta+\bar{\omega}_0t)]\sum_{l'=0}^{\infty}[(\phi_l^{(+)})^*\phi_{l'}^{(+)}C_{l'}^{(+)}+(\phi_l^{(+)})^*\phi_{l'}^{(-)}C_{l'}^{(-)}] \tag{4.4}$$

and

$$-i\frac{\partial C_l^{(-)}(t)}{\partial t}=E_l^{(+)}C_l^{(-)}(t)+E_l^{(-)}C_l^{(+)}(t)$$
$$+\frac{V_b(0)}{\sqrt{2}}\int_0^{2\pi M_a}d\Theta\cos[\nu_0(\Theta+\bar{\omega}_0t)]\sum_{l'=0}^{\infty}[(\phi_l^{(-)})^*\phi_{l'}^{(+)}C_{l'}^{(+)}+(\phi_l^{(-)})^*\phi_{l'}^{(-)}C_{l'}^{(-)}]\ . \tag{4.5}$$

Let is now note that $C_l^{(-)}=C_{-l}^{(+)}$ and $\phi_l^{(-)}=\phi_{-l}^{(+)}$. Then we can write Eqs. (4.4) and (4.5) as a single equation. Let us introduce the function $\phi_p(\Theta)=\phi_{|p|}^{(+)}(\Theta)$ for $p>0$ and $\phi_p(\Theta)=\phi_{-|p|}^{(+)}(\Theta)$ for $p<0$. Similarly we define $C_p(t)=C_{|p|}^{(+)}(t)$ for $p>0$ and $C_P(t)=C_{-|p|}^{(+)}(t)$ for $p<0$. Then Eqs. (4.4) and (4.5) can be written

$$-i\frac{\partial C_p(t)}{\partial t}=E_p^{(+)}C_p(t)+E_p^{(-)}C_{-p}(t)+V_b(0)\int_0^{2\pi M_a}d\Theta\cos[\nu_0(\Theta+\bar{\omega}_0t)]\sum_{p'=-\infty}^{\infty}[(\phi_p)^*\phi_{p'}C_{p'}] \tag{4.6}$$

where the index p has the range $-\infty\le p\le\infty$.

If we expand $\cos[\nu_0(\Theta+\bar{\omega}_0t)]$ in exponentials, we can write Eq. (4.6) in the form

$$-i\frac{\partial C_p(t)}{\partial t}=E_p^{(+)}C_p(t)+E_p^{(-)}C_{-p}(t)+\frac{V_b(0)}{2}\int_0^{2\pi M_a}d\Theta\cos[\nu_0(\Theta+\bar{\omega}_0t)](\phi_p)^*\phi_pC_p(t)$$
$$+\frac{V_b(0)}{2}\sum_{q>0}\{[A(p,p+q)e^{i\nu_0\bar{\omega}_0t}C_{p+q}(t)+A(p,p-q)e^{-i\nu_0\bar{\omega}_0t}C_{p-q}(t)]$$
$$+[B(p,p+q)e^{-i\nu_0\bar{\omega}_0t}C_{p+q}(t)+B(p,p-q)e^{i\nu_0\bar{\omega}_0t}C_{p-q}(t)]\} \tag{4.7}$$

where $q=n/N$ with n an integer,

$$A(p,p\pm q)=\int_0^{2\pi M_a}d\Theta e^{\pm i\nu_0\Theta}[\phi_p(\Theta)]^*\phi_{p\pm q}(\Theta)\ , \tag{4.8}$$

and

$$B(p,p\pm q)=\int_0^{2\pi M_a}d\Theta e^{\mp i\nu_0\Theta}[\phi_p(\Theta)]^*\phi_{p\pm q}(\Theta)\ . \tag{4.9}$$

The equation for $C_p(t)$ contains an infinite number of resonances. [Equation (4.7) and the coefficients $A(p,p\pm q)$ and $B(p,p\pm q)$ were also derived in Ref. 12 although an analytic form of the coefficients was not given.] Resonances with coefficients $A(p,p\pm q)$ lie on the side of the large primary away from the small primary, while resonances with coefficients $B(p,p\pm q)$ lie on the same side of the large primary as the small primary. In Figs. 3–5 we plot some values of the coefficients $B(p,p-q)$ for the special cases $N=1$, $M_a=1$, and $\nu_0=\frac{1}{1}$, $\frac{3}{1}$, and $\frac{5}{1}$. [Note that $B(p,p-q)=B(p+q,p)$.] In Fig. 6 we plot $B(p,p-1)$ and $B(p,p-2)$ for $\nu_0=\frac{5}{1}$, $N=1$, and $V_a(0)=240$. Note that the amplitudes oscillate in the re-

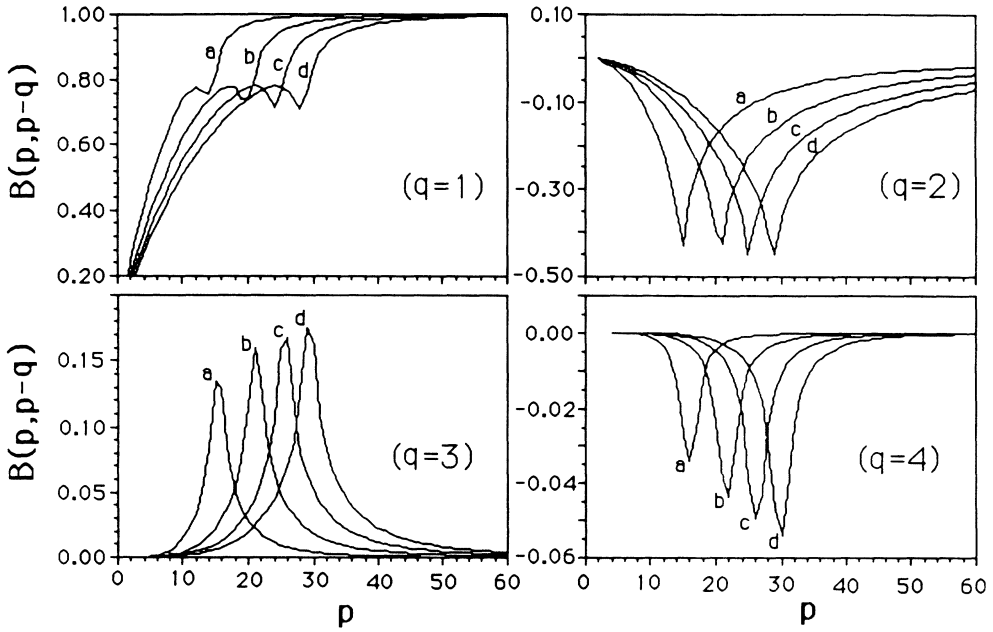

FIG. 3. Plot of amplitudes $B(p,p-q)$ for $\nu_0=\frac{1}{1}$ and $N=1$ for the cases $q=1$–4. In each figure the curves labeled a, b, c, and d correspond to $V_a=240$, 480, 720, and 960, respectively.

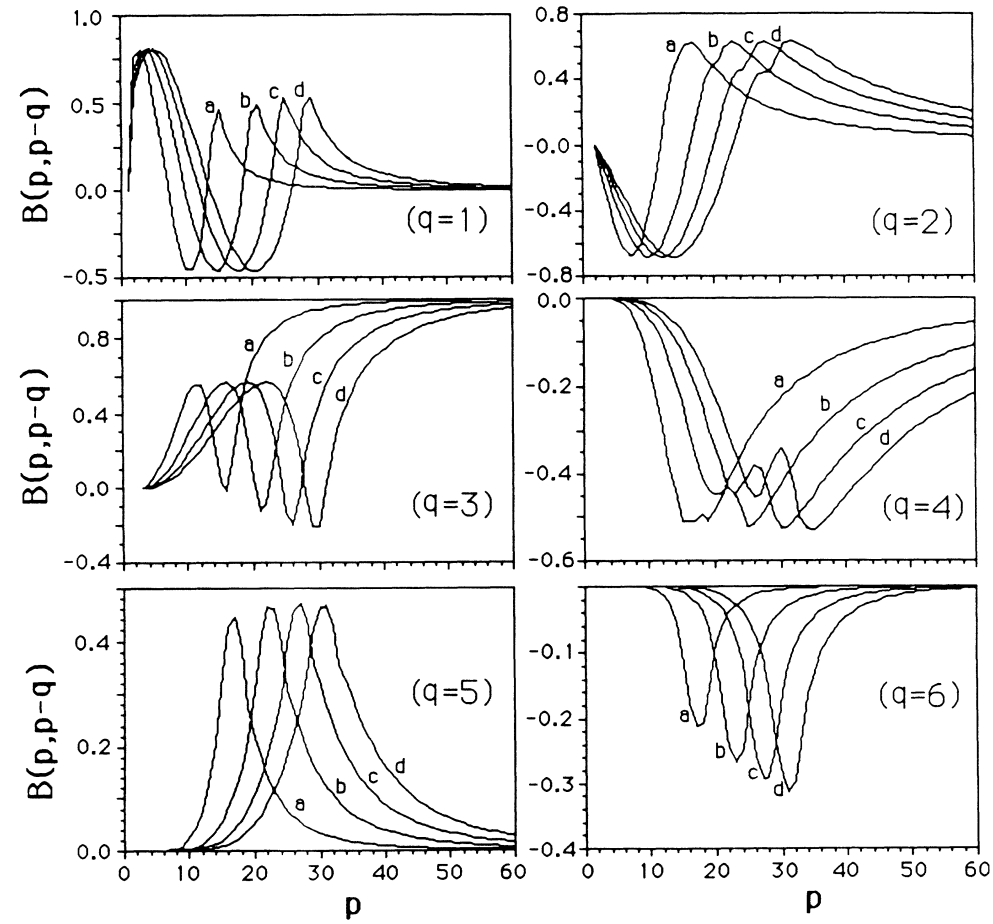

FIG. 4. Plot of amplitudes $B(p,p-q)$ for $\nu_0=\frac{3}{1}$ and $N=1$ for the cases $q=1$–6. In each figure the curves labeled a, b, c, and d correspond to $V_a=240$, 480, 720, and 960, respectively.

gion inside the large primary. This a purely quantum effect. As we showed in Ref. 12 and we shall show below, the coefficients $A(p,p\pm q)$ are extremely small.

We can now use the WKB states derived in Sec. III to obtain explicit expressions for the coefficients $A(p,p\pm q)$ and $B(p,p\pm q)$ for values of $p>[V_a(0)]^{1/2}$. From Eq. (3.7) we find

$$A(p,p\pm q)=\sum_{K=-\infty}^{\infty}\delta_{qN,-M_b\pm KM_a}J_K(x_p-x_{p\pm q}) \tag{4.10}$$

and

$$B(p,p\pm q)=\sum_{K=-\infty}^{\infty}\delta_{qN,M_b\pm KM_a}J_K(x_p-x_{p\pm q}) , \tag{4.11}$$

where K is an integer. Using these results and the fact that $E^{(-)}(p)=0$ for $p>p_c$ (p_c can be determined from Fig. 2), we can rewrite Eq. (4.7) for $p>p_c$:

$$-i\frac{\partial C_P(t)}{\partial t}=p^2C_p(t)+\frac{V_b(0)}{2}\sum_{K=-K^*}^{K^*}[U_K(p)e^{iv_0\bar{\omega}_0t}C_{p-\mu_a(0)(v_0+K)}(t)+U_{-K}(p)e^{-iv_0\bar{\omega}_0t}C_{p+\mu_a(0)(v_0+K)}(t)]+\cdots , \tag{4.12}$$

where the ellipsis represents remaining terms, K^* is the largest integer K such that $p-\mu_a(0)(K+v_0)xp_c$, $U_K(p)=J_K(x_p-x_{p-\mu_0(v_0+K)})$, and $U_{-K}(p)=J_{-K}(x_p-x_{p+\mu_0(v_0+K)})$. Note that $U_{\pm K}(p)=A(p,p\pm q)$ for $-\infty\le K\le-(\text{int}|M_b/M_a|)$ and $U_{\pm K}(p)=B(p,p\pm k)$ for $(\text{int}\,|M_b/M_a|)\le K\le\infty$, where (int $|M_b/M_a|$) indicates the integer part of $|M_b/M_a|+1$.

Let us now note that

$$x_p-x_{p\pm\mu_a(0)(K+v_0)}\approx\pm\frac{(K+v_0)V_a(0)}{2p^2} . \tag{4.13}$$

Thus for $p^2\gg(K+v_0)V_a(0)$ and $K\neq0$ we have

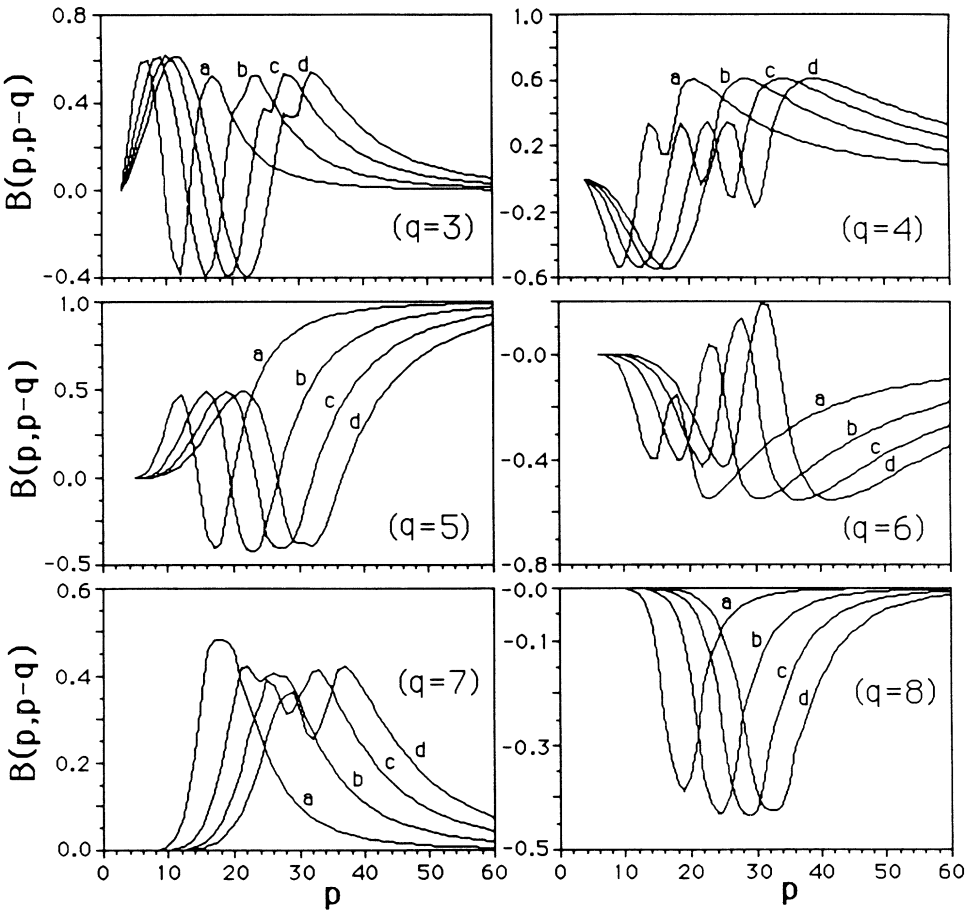

FIG. 5. Plot of amplitudes $B(p,p-q)$ for $v_0=\frac{5}{1}$ and $N=1$ for the cases $q=3$–8. In each figure the curves labeled a, b, c, and d correspond to $V_a=240$, 480, 720, and 960, respectively.

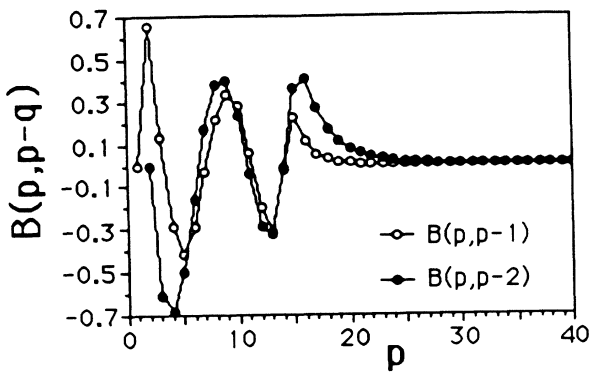

FIG. 6. Plot of amplitudes $B(p,p-1)$ and $B(p,p-2)$ for $\nu_0=\frac{5}{1}$ and $N=1$ for the case $V_a=240$.

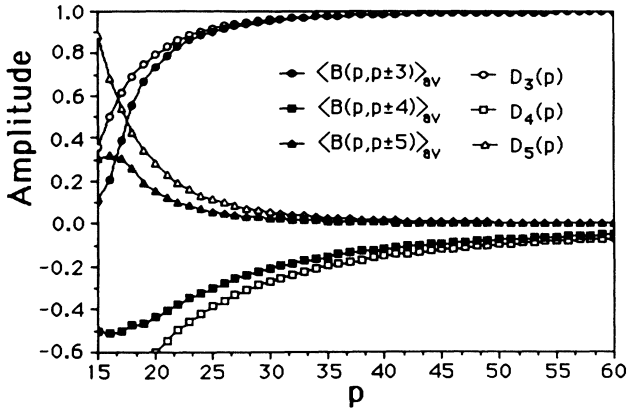

FIG. 8. A comparison of $\langle B(p,p\pm q)\rangle_{\rm av}$ vs p and $D_{\nu_0+q-1}(p)$ vs p for $\nu_0=\frac{3}{1}$, $N=1$, and $V_a=240$, for the cases $q=3,4,5$.

$$J_{\pm K}(x_p-x_{p\mp\mu_a(0)(K+\nu_0)})\approx\frac{(-1)^K}{2|K|\,|K|!}\left[\frac{(\nu_0+K)V_a(0)}{2p^2}\right]^{|K|}\equiv D_{K+\nu_0}(p)\ . \tag{4.14}$$

For $K=0$ we find

$$J_0(x_p-x_{p\pm\nu_0\mu_a(0)})\approx 1-\frac{1}{4}\left[\frac{(\nu_0)^2[V_a(0)]^2}{4p^4}\right]\equiv D_{\nu_0}(p)\ . \tag{4.15}$$

Using the above coefficients, we can write Eq. (4.12) in the form (for $p>p_c$)

$$-i\frac{\partial C_p^{(0)}(t)}{\partial t}=p^2C_p^{(0)}(t)+\frac{V_b(0)}{2}\sum_{K=-K^*}^{K^*}D_{K+\nu_0}(p)[C^{(0)}_{p-\mu_a(0)(K+\nu_0)}(t)e^{i\nu_0\bar\omega_0 t}+C^{(0)}_{p+\mu_0(0)(K+\nu_0)}(t)e^{-i\mu_a(0)\bar\omega_0 t}]+\cdots\ . \tag{4.16}$$

In Figs. 7–9, we compare the average amplitude $\langle B(p,p\pm q)\rangle_{\rm av}=\frac{1}{2}[B(p,p-q)+B(p,p+q)]$ for $\nu_0=\frac{1}{1}$, $\frac{3}{1}$, and $\frac{5}{1}$, $N=1$, $M_a(0)=1$, with the approximate amplitudes D_K. We see that the WKB approximations are fairly good although they tend to overestimate the amplitude as we get too close to the edge of the large primary resonance. However, this is where we expect the WKB approximation to begin to break down.

In Eq. (4.16), the Kth resonance is located at

$$\bar p_K=-\frac{\nu_0\bar\omega_0}{2\mu_a(0)(K+\nu_0)}\ . \tag{4.17}$$

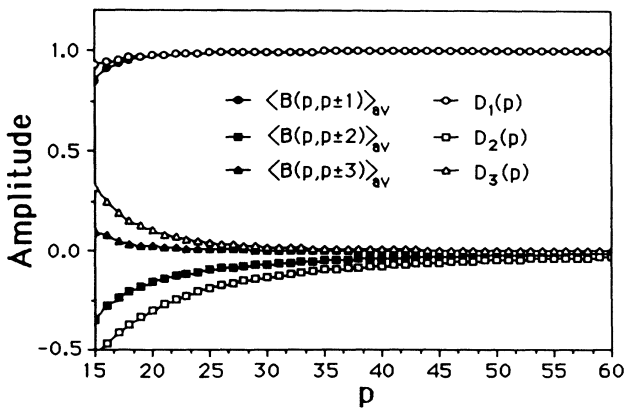

FIG. 7. A comparison of $\langle B(p,p\pm q)\rangle_{\rm av}$ vs p and $D_{\nu_0+q-1}(p)$ vs p for $\nu_0=\frac{1}{1}$, $N=1$, and $V_a=240$, for the cases $q=1,2,3$.

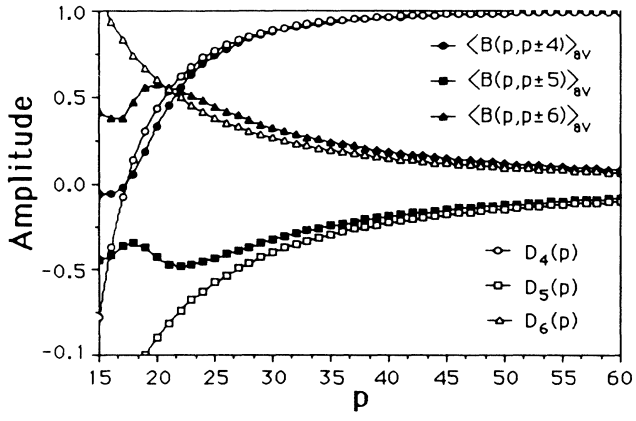

FIG. 9. A comparison of $\langle B(p,p\pm q)\rangle_{\rm av}$ vs p and $D_{\nu_0+q-1}(p)$ vs p for $\nu_0=\frac{5}{1}$, $N=1$, and $V_a=240$, for the cases $q=4,5,6$.

We will now evaluate the amplitude of the Kth resonance at the position of the Kth resonance. Then we can write $D_{K+\nu_0}(p) \approx D_{K+\nu_0}(p_K)$. (The validity of this approximation was discussed in Ref. 12.) Let us now make this substitution in Eq. (4.16) and write it in terms of angle variables. We will let

$$\langle \theta|\Psi^{(1)}(t)\rangle = \sum_{p=-\infty}^{\infty} C_p^{(0)}(t) e^{ip\theta} . \tag{4.18}$$

Since $p = m/N$, where m is an integer, the wave function $\langle \theta|\Psi^{(1)}(t)\rangle$ satisfies the periodic boundary conditions $\langle \theta|\Psi^{(1)}(t)\rangle = \langle \theta + 2\pi N|\Psi^{(1)}(t)\rangle$. Using Eq. (4.18), we obtain

$$-i\frac{\partial\langle \theta|\Psi^{(1)}(t)\rangle}{\partial t} = -\frac{\partial^2\langle \theta|\Psi^{(1)}(t)\rangle}{\partial\theta^2} + V_b(0)\sum_{K=-K^*}^{K^*} D_{K+\nu_0}(p_K)\cos[\mu_a(0)(K+\nu_0)\theta + \nu_0\bar{\omega}_0 t]\langle \theta|\Psi^{(1)}(t)\rangle + \cdots . \tag{4.19}$$

Equation (4.19) is a Schrödinger equation which describes the state of the system in a basis consisting of eigenstates of the large primary resonance. It is very similar to Eq. (2.1) in structure except that it contains an infinite number of resonances. We shall select two of these as the next step in our renormalization transformation.

V. RENORMALIZATION TRANSFORMATION

Having obtained the Schrödinger equation for secondary resonances, we will now select a pair of neighboring resonances and write the paradigm Schrödinger equation for this resonance pair. This will give us the renormalization mapping on the relative wave numbers and amplitudes of an arbitrary sequence of resonance pairs.

A. Renormalization mapping

Let us now select two neighboring resonance terms, $K = N_1$ and $K = N_1 + 1$ in Eq. (4.19). Then we obtain the following double-resonance Schrödinger equation:

$$\begin{aligned} -i\frac{\partial\langle \theta|\Psi^{(1)}(t)\rangle}{\partial t} = &-\frac{\partial^2\langle \theta|\Psi^{(1)}(t)\rangle}{\partial\theta^2} + V_b(0)D_{N_1+\lambda_1+\nu_0}(p_{N_1+\lambda_1})\cos[\mu_a(0)(M_1+\lambda_1+\nu_0)\theta + \nu_0\bar{\omega}_0 t] \\ &+ V_b(0)D_{N_1+1-\lambda_1+\nu_0}(p_{N_1+1-\lambda_1})\cos[\mu_a(0)(M_1+1-\lambda_1+\nu_0)\theta + \nu_0\bar{\omega}_0 t] . \end{aligned} \tag{5.1}$$

We have included a factor λ_1, where $\lambda_1 = 0$ or 1, in Eq. (5.1) so that at subsequent steps of the renormalization transformation we can choose either of the two resonances as a basis for building the WKB solutions. We can rewrite Eq. (5.1) in the form

$$-i\frac{\partial\langle \theta|\Psi^{(1)}(t)\rangle}{\partial t} = -\frac{\partial^2\langle \theta|\Psi^{(1)}(t)\rangle}{\partial\theta^2} + \{V_a(1)\cos[\mu_a(1)\theta - \omega_1 t] + V_b(1)\cos[\mu_b(1)\theta - \omega_1 t]\}\langle \theta|\Psi_1(t)\rangle \tag{5.2}$$

where $V_a(1) = V_b(0)D_{N_1+\lambda_1+\nu_0}(p_{N_1+\lambda_1})$, $V_b(1) = V_b(0)D_{N_1+1-\lambda_1+\nu_0}(p_{N_1+1-\lambda_1})$, $\mu_a(1) = \mu_a(0)(N_1+\lambda_1+\nu_0)$, $\mu_b(1) = \mu_a(0)(N_1+1-\lambda_1+\nu_0)$, $\omega_1 = -\nu_0\bar{\omega}_0$.

Equation (5.2) now has the same form as Eq. (2.1) and we can use the same procedure as in Sec. II to write it in the form of a paradigm Schrödinger equation. We find

$$-i\frac{\partial\langle \Theta|\chi^{(1)}(t)\rangle}{\partial t} = -\mu_a(1)^2\frac{\partial^2\langle \Theta|\chi^{(1)}(t)\rangle}{\partial\Theta^2} + \{V_a(1)\cos(\Theta) + V_b(1)\cos[\nu_1(\Theta + \bar{\omega}_1 t)]\}\langle \Theta|\chi^{(1)}(t)\rangle \tag{5.3}$$

where

$$\nu_1 = \frac{\mu_b(1)}{\mu_a(1)} = \frac{N_1+1-\lambda_1+\nu_0}{N_1+\lambda_1+\nu_0} \text{ and } \bar{\omega}_1 = \frac{(\nu_1-1)}{\nu_1}\omega_1 . \tag{5.4}$$

The cosine waves in Eq. (5.3) have speed $\dot{\Theta} = 0$ and $\dot{\Theta} = -\bar{\omega}_1$. The resonance condition places the resonances that result from these cosine waves at $\bar{p} = 0$ and $\bar{p} = -\bar{\omega}_1/2M_a(1)^2$, respectively. Thus they are separated by a distance $\bar{\omega}_1/2M_a(1)^2$. The half-width of the ith resonance is $\Delta p_i = [2V_i(1)]^{1/2}$ $(i = a,b)$.[3,4] The Chirikov condition for overlap of the two resonances in Eq. (5.3) is given by $[2V_a(1)]^{1/2} + [2V_b(1)]^{1/2} = \bar{\omega}_1/2M_a(1)^2$. Let us introduce two new variables, $X(1)$ and $Y(1)$ defined $X(1) = 2M_a(1)[2V_a(1)]^{1/2}/\bar{\omega}_1$ and $Y(1) = 2M_a(1)[2V_b(1)]^{1/2}/\bar{\omega}_1$. Then the Chirikov criterion is $X(1) + Y(1) = 1$. Note that the amplitudes, X and Y, are independent of $\hbar$.

The renormalization transformations can be expressed in the following form in going from the αth to the $(\alpha+1)$st paradigm Schrödinger equation. The wave number transforms as

$$\nu_{\alpha+1} = \frac{N_{\alpha+1}+1-\lambda_{\alpha+1}+\nu_\alpha}{N_{\alpha+1}+\lambda_{\alpha+1}+\nu_\alpha} . \tag{5.5}$$

The frequency transforms as

$$\bar{\omega}_{\alpha+1}=-\frac{\nu_{\alpha+1}-1}{\nu_{\alpha+1}}\nu_\alpha\bar{\omega}_\alpha\ . \tag{5.6}$$

The mapping of $X(\alpha)$ and $Y(\alpha)$ from the αth level to the $\alpha+1$ level is given by

$$X^2(\alpha+1)=\frac{(-1)^{N_{\alpha+1}+\lambda_{\alpha+1}}}{2^{N_{\alpha+1}+\lambda_{\alpha+1}}(N_{\alpha+1}+\lambda_{\alpha+1})!}\left[\frac{(N_{\alpha+1}+1-\lambda_{\alpha+1}+\nu_\alpha)^2(N_{\alpha+1}+\lambda_{\alpha+1}+\nu_\alpha)^2}{\nu_\alpha^2}\right]$$
$$\times Y(\alpha)^2\left[\frac{(N_{\alpha+1}+\lambda_{\alpha+1}+\nu_\alpha)^3X(\alpha)^2}{4\nu_\alpha^2}\right]^{N_{\alpha+1}+\lambda_{\alpha+1}}\quad\text{for } N_{\alpha+1}+\lambda_{\alpha+1}\neq 0\ , \tag{5.7a}$$

$$X^2(\alpha+1)=\left[\frac{(N_{\alpha+1}+1-\lambda_{\alpha+1}+\nu_\alpha)^2(N_{\alpha+1}+\lambda_{\alpha+1}+\nu_\alpha)^2}{\nu_\alpha^2}\right]Y(\alpha)^2\left[1-\left[\frac{\nu_\alpha^2X^4(\alpha)}{64}\right]\right]\quad\text{for } N_{\alpha+1}+\lambda_{\alpha+1}=0\ , \tag{5.7b}$$

and

$$Y^2(\alpha+1)=\frac{(-1)^{N_{\alpha+1}+1-\lambda_{\alpha+1}}}{2^{N_{\alpha+1}+1-\lambda_{\alpha+1}}(N_{\alpha+1}+1-\lambda_{\alpha+1})!}\left[\frac{(N_{\alpha+1}+1-\lambda_{\alpha+1}+\nu_\alpha)^2(N_{\alpha+1}+\lambda_{\alpha+1}+\nu_\alpha)^2}{\nu_\alpha^2}\right]$$
$$\times Y(\alpha)^2\left[\frac{(N_{\alpha+1}+1-\lambda_{\alpha+1}+\nu_\alpha)^3X(\alpha)^2}{4\nu_\alpha^2}\right]^{N_{\alpha+1}+1-\lambda_{\alpha+1}}\quad\text{for } N_{\alpha+1}+1-\lambda_{\alpha+1}\neq 0\ , \tag{5.8a}$$

$$Y^2(\alpha+1)=\left[\frac{(N_{\alpha+1}+1-\lambda_{\alpha+1}+\nu_\alpha)^2(N_{\alpha+1}+\lambda_{\alpha+1}+\nu_\alpha)^2}{\nu_\alpha^2}\right]Y(\alpha)^2\left[1-\left[\frac{\nu_\alpha^2X^4(\alpha)}{64}\right]\right]$$
$$\text{for } N_{\alpha+1}+1-\lambda_{\alpha+1}=0\ . \tag{5.8b}$$

The mappings in Eqs. (5.5)–(5.8) allow us to determine whether or not any given sequence of resonance pairs overlap as we go to small scale in the Hilbert space. A particular sequence is determined once we fix λ_α and N_α at each scale. If overlap has occurred between all sequences of higher-order resonance pairs between the two primary resonances, then we know that there is a continual path for probability to flow between the two primary resonances. The possibility of mappings such as those in Eqs. (5.5)–(5.8) has been proposed by Berman and Kolovsky,[13] however no explicit expressions were given.

B. Fixed points of wave-number mapping

The wave-number mapping, Eq. (5.5), can be studied independently of the amplitude mapping Eqs. (5.7) and (5.8) and determines the particular sequence of resonance pairs that is followed in the amplitude mappings. The relative wave number ν_α at the αth level of the renormalization transformation is determined by the sequence of values, $N_{\alpha'}$ and $\lambda_{\alpha'}$ ($\alpha'\leq\alpha$), that precede it. Thus we can write ν_α schematically in the form

$$\nu_\alpha=\{N_\alpha,\lambda_\alpha;N_{\alpha-1},\lambda_{\alpha-1};\ldots;N_1,\lambda_1;\nu_0\}$$

For the special cases in which λ_α is fixed to be either 0 or 1 for all α, ν_α can be written as a continued fraction. Let us consider these two cases separately.

Case (i) ($\lambda_\alpha=0$ *for all* α). For this case the relative wave number can be written as the continued fraction

$$\begin{aligned}\nu_\alpha&=\{N_\alpha,0;N_{\alpha-1},0;\ldots;N_1,0;\nu_0\}=1+\frac{1}{N_\alpha+\nu_{\alpha-1}}\\&=[1,N_\alpha+1,N_{\alpha-1}+1,\ldots,N_2+1,N_1+\nu_0]\\&\equiv 1+\cfrac{1}{N_\alpha+1+\cfrac{1}{N_{\alpha-1}+1+\cdots\cfrac{1}{N_1+\nu_0}}}\ .\end{aligned} \tag{5.9}$$

For the special case $N_\alpha=n$ for all α the mapping has fixed points $\bar{\nu}_n^{(0)}=\frac{1}{2}[1-n+(n^2+2n+5)^{1/2}]$, where $n\geq 0$. $\bar{\nu}_n^{(0)}$ can be expressed as a continued fraction

$$\bar{\nu}_n(\lambda=0)=[1,n+1,n+1,\ldots]\ . \tag{5.10}$$

For $n=0$ this is just the golden mean, $\nu_0^{(0)}=\gamma=[(1+\sqrt{5}/2)]$.

Case (ii) ($\lambda_\alpha=1$ *for all* α). For this case the relative wave number can be written as the continued fraction

$$\begin{aligned}\nu_\alpha&=\{N_\alpha,1;N_{\alpha-1},1;\ldots;N_1,1;\nu_0\}\\&=\frac{N_\alpha+\nu_{\alpha-1}}{N_\alpha+\nu_{\alpha-1}+1}\\&\equiv[0,1,N_\alpha,1,N_{\alpha-1},1,\ldots,N_2,1,N_1+\nu_0]\ .\end{aligned}$$

For the case $N_\alpha=n$ for all α, the mapping for the relative wave number takes the form

$$\nu_{\alpha+1}=\frac{\nu_\alpha+n}{\nu_\alpha+n+1}=\frac{1}{1+\dfrac{1}{n+\nu_\alpha}}\ . \tag{5.11}$$

This equation has fixed points at $\bar{\nu}_n^{(1)}=\frac{1}{2}[-n+(n^2+4n)^{1/2}]$ with $n\geq 1$. If we iterate Eq. (5.11), we find that $\bar{\nu}_n^{(1)}$ can be expressed as a continued fraction

$$\bar{\nu}_n^{(1)}=[0,1,n,1,n,\ldots]=\cfrac{1}{1+\cfrac{1}{n+\cfrac{1}{1+\cdots}}} . \quad (5.12)$$

For $n=1$ this is just the inverse golden mean, $\bar{\nu}_1^{(1)}=[(\sqrt{5}-1)/2]$. Continued fractions with the structure $[a_0,a_1,\ldots,a_n,1,1,\ldots]$ define "noble" resonance sequences. It appears that the noble resonance sequences in the quantum case are often the last to overlap as is true classically. This can be seen by studying the stable manifolds that result from the mappings Eqs. (5.7) and (5.8).

C. Stable manifolds

We have studied the mapping Eqs. (5.5)–(5.8) for three different choices of the primary resonances. We have taken $N=1$ and have considered $\nu_0=\frac{1}{1}[\mu_a(0)=1,\mu_b(0)=1]$, $\nu_0=\frac{3}{1}[\mu_a(0)=1,\mu_b(0)=3]$, and $\nu_0=\frac{5}{1}[\mu_a(0)=1,\mu_b(0)=5]$. In terms of our original traveling-wave basis, the large primary resonance is centered at $\bar{k}_a=\omega_0/2\mu_a(0)$ while the small primary lies at $\bar{k}_b=\omega_0/2\mu_b(0)$. After the first step of the renormalization transformation, in which we expand the Schrödinger equation in terms of the eigenstates of the large primary resonance, we obtain an infinite number of secondary resonances whose relative wave numbers are given by

$$\nu_1=\left\lfloor \frac{N_1+1+\nu_0}{N_1+\nu_0} \right\rfloor$$

where $-\infty\leq N_1\leq\infty$. These secondary resonances are located in the Hilbert space of eigenstates of the large primary at

$$\bar{p}_{N_1}=-\frac{\nu_0\bar{\omega}_0}{2\mu_a(0)(N_1+\nu_0)} .$$

For $\bar{p}_{N_1}\gg[2V_a(0)]^{1/2}$, we can locate these resonances in the original Hilbert space at

$$\bar{k}_{N_1}\approx\bar{p}_{N_1}+\bar{k}_a$$

since far from the large primary resonance the eigenstates become approximately traveling waves. Let us now consider the three cases $\nu_0=\frac{1}{1}$, $\nu_0=\frac{3}{1}$, $\nu_0=\frac{5}{1}$ separately.

Case (i) ($\nu_0=\frac{1}{1}$). For the case $\nu_0=\frac{1}{1}$ we must choose the plus sign in the cosine wave, $\cos[\mu_b(0)\theta\pm\omega_0 t]$, Eq. (2.1). Thus $\bar{\omega}_0=[(\nu_0+1)/\nu_0]\omega_0=2\omega_0$. The mapping equations contain stable manifolds which separate values of $X(0)$ and $Y(0)$ for which a sequence resonance pairs overlap and for which they do not.

The two primary resonances (shaded) and two pairs of secondary resonances are shown schematically in Fig. 10 (the small primary becomes a secondary). If $N_1=0$ and $\lambda=0$, then $\nu_1=\frac{2}{1}$. The two resonances forming this resonance pair are located at $\bar{p}_0=-\omega_0$ and $\bar{p}_1=-\omega_0/2$ (or

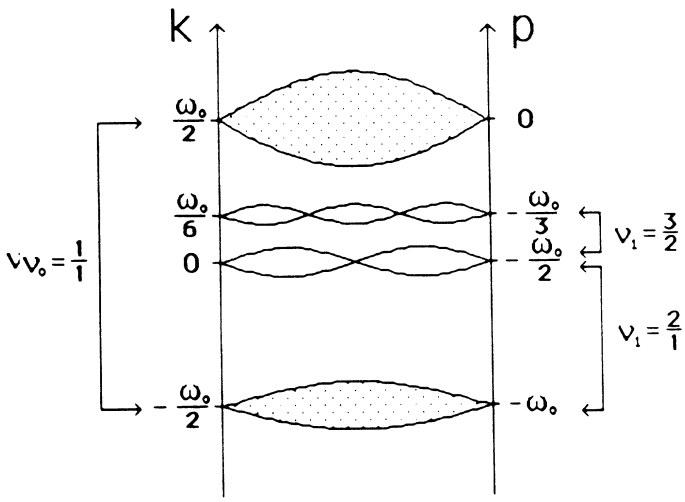

FIG. 10. A sketch of resonance pairs for $\nu_0=\frac{1}{1}$ and $\nu_1=\frac{2}{1}$ and $\nu_1=\frac{3}{2}$. The relative spacings and wave numbers are shown accurately but the sizes are not to scale.

$\bar{k}_0\approx-\omega_0/2$ and $\bar{k}_1\approx 0$). The two resonances corresponding to $N_1=1$ and $\lambda=0$ have relative wave number $\nu_1=\frac{3}{2}$. They are located at $\bar{p}_1=0$ and $\bar{p}_2=\omega_0/6$ (or $\bar{k}_0\approx-\omega_0/2$ and $\bar{k}_1\approx-\omega_0/3$). The mapping must be performed so that at each step, the larger of the two resonances is used to determine $X(\alpha)$ and the smaller determines $Y(\alpha)$.

We have searched for overlap of a large variety of resonance sequences. We find stable manifolds separating the stable region of values $(X(0),Y(0))$ for which no overlap occurs as we go to smaller scale [that is, $X(\alpha)\to 0$ and $Y(\alpha)\to 0$ as $\alpha\to\infty$], from the unstable region in which overlap does occur as we go to smaller scale [$X(\alpha)\to\infty$ and $Y(\alpha)\to\infty$ as $\alpha\to\infty$]. Once we cross the stable manifold from the stable to the unstable side, the growth in $X(\alpha)$ and $Y(\alpha)$ is rapid. We were interested in predicting the values $(X(0),Y(0))$ at which overlap of the resonance pair $\nu_1=\frac{2}{1}$ occurs. This happens when all resonance sequences starting from the pair $\nu_1=\frac{2}{1}$ have overlapped. We found that there was a significant range of values for which we could maintain $X(\alpha)>Y(\alpha)$ with $\lambda_\alpha=0$ for all α. In Fig. 11, we show the stable manifolds corresponding to sequences (with $\lambda_\alpha=0$ for all α) $\nu=[1,0,0,\ldots,0,0,\frac{1}{1}]$, $\nu=[1,1,1,\ldots,1,0,\frac{1}{1}]$, and $\nu=[1,2,2,\ldots,2,0,\frac{1}{1}]$ [these correspond to $\nu_1=\frac{2}{1}$ and (a), (b), and (c), respectively, in Fig. 11]. We also studied overlap of the resonance pair $\nu_1=\frac{3}{2}$. In Fig. 11 we show stable manifolds for sequences $\nu=[1,0,0,\ldots,0,1,\frac{1}{1}]$, $\nu=[1,1,1,\ldots,1,1,\frac{1}{1}]$, and $\nu=[1,2,2,\ldots,2,1,\frac{1}{1}]$ [these correspond to $\nu_1=\frac{3}{2}$ and (d), (e), and (f), respectively, in Fig. 11]. It is interesting that these sequences each correspond to the last [for increasing $X(0)$ and $Y(0)$] overlapping sequence for some range of $X(0)$ and $Y(0)$. Note that as $X(0)$ and $Y(0)$ become roughly equal, the sequences $\nu=[1,0,0,\ldots,0,0,\frac{1}{1}]$ and $\nu=[1,0,0,\ldots,0,1,\frac{1}{1}]$ which are noble sequences are the last to overlap. In this case we approach the standard map. Also, note that overlap between resonance pair $\nu_1=\frac{3}{2}$ occurs for smaller values of

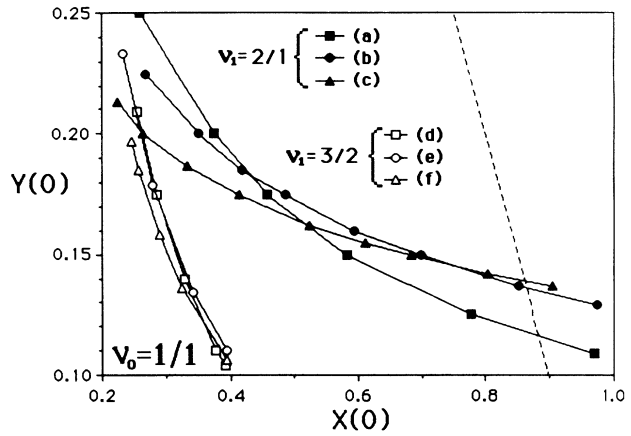

FIG. 11. Some stable manifolds for $\nu_1=\frac{1}{1}$. Solid symbols indicate curves for $\nu_1=\frac{2}{1}$ and (a) $n_\alpha=0$ for $\alpha>1$, (b) $n_\alpha=1$ for $\alpha>1$, and (c) $n_\alpha=2$ for $\alpha>1$. Open symbols indicate curevs for $\nu_1=\frac{3}{2}$ and (d) $n_\alpha=0$ for $\alpha>1$, (e) $n_\alpha=1$ for $\alpha>1$, and (f) $n_\alpha=2$ for $\alpha>1$. The dashed line is the Chirikov prediction, $X(0)+Y(0)=1$.

$X(0)$ and $Y(0)$ than does overlap of resonance pair $\nu_1=\frac{2}{1}$.

Case (ii) ($\nu_0=\frac{3}{1}$). For this case, $\bar{\omega}_0=[(\nu_0-1)/\nu_0]\omega_0=\frac{2}{3}\omega_0$. In Fig. 12, we have given a sketch of the two primary resonances (shaded) and two pairs of secondary resonances $\nu_1=\frac{4}{3}(N_1=0)$ and $\nu_1=\frac{5}{4}(N_1=1)$. Again, we show the relative wave numbers and positions of the resonances accurately but the width of the secondaries is exaggerated. For this case, the secondary pairs are much closer together than for the case $\nu_0=\frac{1}{1}$ and lie further from the large primary. In Fig. 13, we show the stable manifolds for the last [as $X(0)$ and $Y(0)$ increase] resonance sequences to overlap for the resonance pairs $\nu_1=\frac{4}{3}$, $\frac{5}{4}$, $\frac{6}{5}$, and $\frac{7}{6}$. For these four cases the resonance sequences were given by $\lambda_\alpha=0$ for all α and $\nu=[1,0,0,\ldots,0,0,\frac{3}{1}]$, $\nu=[1,0,0,\ldots,0,1,\frac{3}{1}]$,

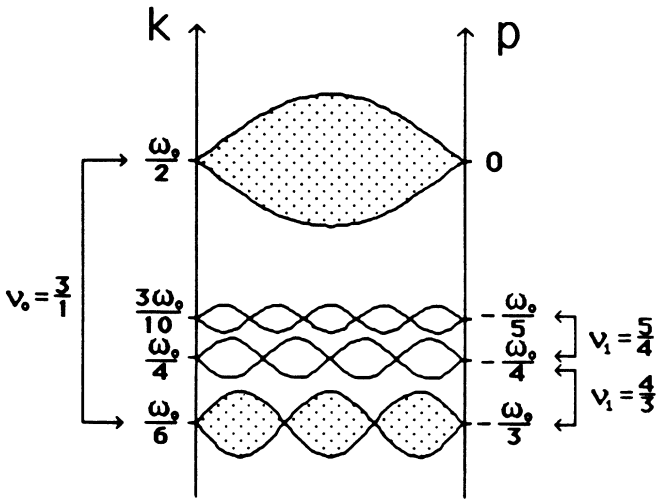

FIG. 12. A sketch of resonance pairs for $\nu_0=\frac{3}{1}$ and $\nu_1=\frac{4}{3}$ and $\nu_1=\frac{5}{4}$. The relative spacings and wave numbers are shown accurately but the sizes are not to scale.

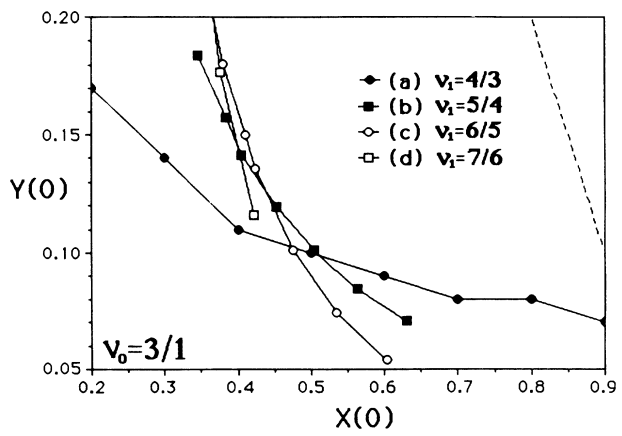

FIG. 13. Some stable manifolds for $\nu_1=\frac{3}{1}$. For all curves shown, $n_\alpha=0$ for $\alpha>1$. The dashed line is the Chirikov prediction, $X(0)+Y(0)=1$.

$\nu=[1,0,0,\ldots,0,2,\frac{3}{1}]$, and $\nu=[1,0,0,\ldots,0,3,\frac{3}{1}]$, respectively. Thus, the noble resonance sequences in these cases were the last to overlap.

In Figs. 14 and 15, we show additional stable manifolds for the cases $\nu_1=\frac{4}{3}$ and $\nu_1=\frac{5}{4}$. In Fig. 14, we show stable manifolds for the sequences (a) $\nu=[1,0,0,\ldots,0,0,\frac{3}{1}]$, (b) $\nu=[1,1,1,\ldots,1,0,\frac{3}{1}]$, and (c) $\nu=[1,2,2,\ldots,2,0,\frac{3}{1}]$ for the resonance pair $\nu_1=\frac{4}{3}$. Clearly the noble resonance sequences are the last to overlap. In Eq. (5.6), we show the stable manifolds for the sequences (a) $\nu=[1,0,0,\ldots,0,1,\frac{3}{1}]$, (b) $\nu=[1,1,1,\ldots,1,1,\frac{3}{1}]$, and (c) $\nu=[1,2,2,\ldots,2,1,\frac{3}{1}]$ for the resonance pair $\nu_1=\frac{5}{4}$. Again, the noble resonance sequences are the last to overlap over the range of $X(0)$ and $Y(0)$ for which our theory is valid.

Case (iii) ($\nu_0=\frac{5}{1}$). For this case, $\bar{\omega}_0=[(\nu_0-1)/\nu_0]\omega_0=\frac{4}{5}\omega_0$. in Fig. 16, we show a sketch of the two primary resonances (shaded) and two pairs of secondary resonances $\nu_1=\frac{6}{5}(N_1=0)$ and $\nu_1=\frac{7}{6}(N_1=1)$. The relative wave numbers and positions of the resonances are given accurately but the width of the secondaries is exaggerated. For this case, the secondary pairs are still farther

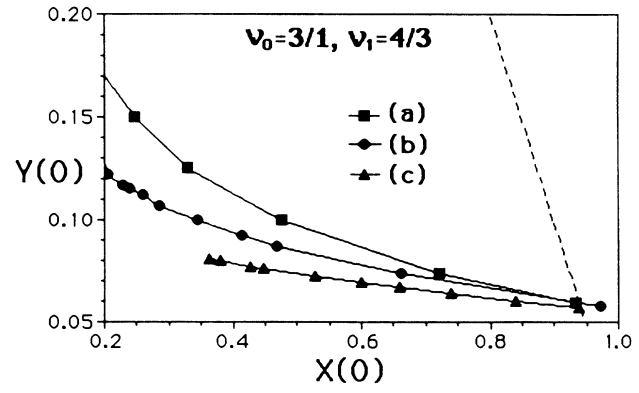

FIG. 14. Some stable manifolds for $\nu_0=\frac{3}{1}$. and $\nu_1=\frac{4}{3}$ and (a) $n_\alpha=0$ for $\alpha>1$, (b) $n_\alpha=1$ for $\alpha>1$, and (c) $n_\alpha=2$ for $\alpha>1$. The dashed line is the Chirikov prediction, $X(0)+Y(0)=1$.

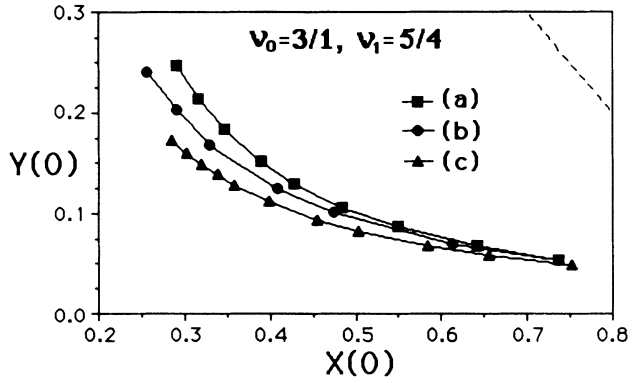

FIG. 15. Some stable manifolds for $\nu_0=\frac{3}{1}$. and $\nu_1=\frac{5}{4}$ and (a) $n_\alpha=0$ for $\alpha>1$, (b) $n_\alpha=1$ for $\alpha>1$, and (c) $n_\alpha=2$ for $\alpha>1$. The dashed line is the Chirikov prediction, $X(0)+Y(0)=1$.

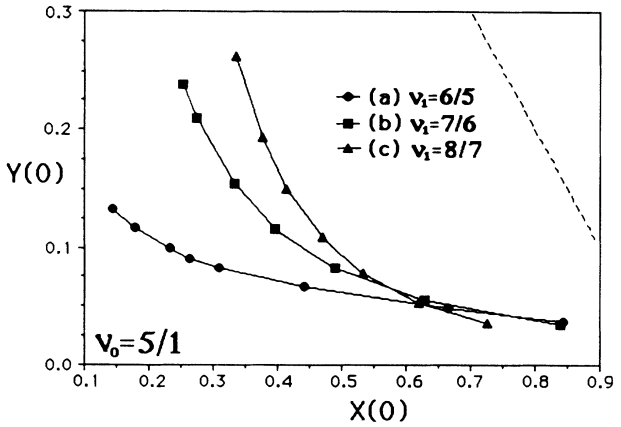

FIG. 17. Some stable manifolds for $\nu_0=\frac{5}{1}$. For all curves shown, $n_\alpha=0$ for $\alpha>1$. The dashed line is the Chirikov prediction, $X(0)+Y(0)=1$.

away from the large primary than was the case for $\nu_0=\frac{1}{1}$ or $\nu_0=\frac{3}{1}$. The stable manifolds for the last resonance sequences to overlap for the resonance pairs $\nu_1=\frac{6}{5}$, $\frac{7}{6}$, and $\frac{8}{7}$ are shown in Fig. 17. These stable manifolds correspond to $\lambda_\alpha=0$ for all α and (a) $\nu=[1,0,0,\ldots,0,0,\frac{5}{1}]$, (b) $\nu=[1,0,0,\ldots,0,1,\frac{5}{1}]$, and (c) $\nu=[1,0,0,\ldots,0,2,\frac{5}{1}]$. Other sequences we studied had stable manifolds lying at lower values of $X(0)$ and $Y(0)$ than did these resonance pairs.

VI. NUMERICAL DISCUSSION

There have been a number of studies which indicate that resonance overlap in quantum systems can lead to a fairly abrupt spreading of probability over the region of Hilbert space which is influenced by the resonances.[9,10] There is also evidence of KAM behavior.[6] That is, blockages to the spread of probability which in classical systems would be attributed to KAM surfaces. Probability appears to decay exponentially across these barriers.

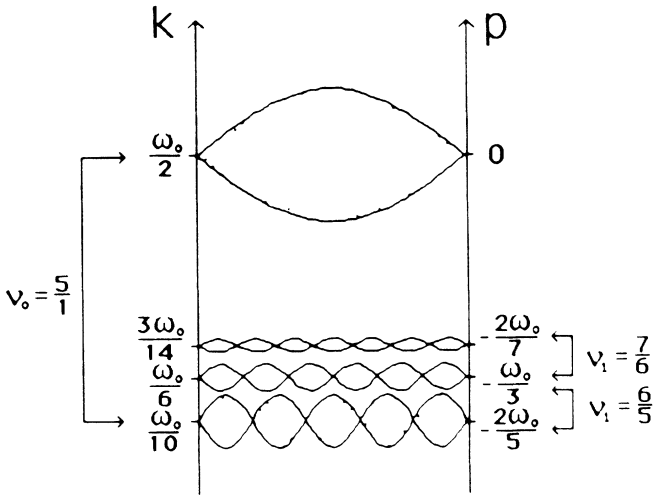

FIG. 16. A sketch of resonance pairs for $\nu_0=\frac{5}{1}$ and $\nu_1=\frac{6}{5}$ and $\nu_1=\frac{7}{6}$. The relative spacings and wave numbers are shown accurately but the sizes are not to scale.

We have considered two cases, $\omega_0=120$ and $\omega_0=240$, of the double-resonance model with $N=1$, $\mu_a(0)=1$, and $\mu_b(0)=3$ for both cases (this was also studied in Ref. 12), and we have compared the predictions of the renormalization transformation with the actual spread of probability. The effect of increasing the frequency ω_0 is to move the primary resonances farther apart and this also increases the number of states between the two primaries. Once we fix the frequency ω_0 the positions of the primaries are fixed. However, we can still adjust their size. In the following we will fix the size of the small primary and adjust the size of the large primary. We start with all the probability initially on the state at the center of the small primary and we then integrate the equations of motion, Eq. (2.2), for a long time (many periods $T=2\pi/\omega_0$) to determine how far the probability can spread. We typically find that after a few periods the probability reaches its maximum extent and does not spread further although it may slosh around within the region in which it is confined. The manner in which the probability spreads gives us some idea about the nature of the barriers and/or resonances that lie in its path. In order to attempt to eliminate local fluctuations due to sloshing we have computed the spread after ten different times and have averaged over those ten different sets of values according to the equation

$$\bar{P}_k=\frac{1}{10}\sum_{j=1}^{5}[|\Psi_k^{(0)}(2j)|^2+|\Psi_k^{(0)}(2.3j)|^2]\,, \tag{6.1}$$

where $\Psi_k^{(0)}(t)$ is the solution of Eq. (2.2) at time t assuming initial conditions $|\Psi_{\bar{k}_b}^{(0)}(0)|^2=1$ and $|\Psi_k^{(0)}(0)|^2=0$ for $k\neq\bar{k}_b$.

For the case when $\omega_0=120$ we fix $V_b(0)=20$ and find $Y(0)=0.158$, while for the case $\omega_0=240$ we fix $V_b(0)=80$ and again find $Y(0)=0.158$. From Fig. 13, we expect overlap of the resonance pair $\nu_1=\frac{4}{3}$ to occur for $X(0)=0.23$, while for resonance pair $\nu_1=\frac{5}{4}$ we expect overlap to occur for $X(0)=0.4$. We will now show how the probability spreads through these two regions and

compare this spread with the predictions of the renormalization transformation. We will first consider the case when $\omega_0=120$.

Case I ($\omega_0=120$, $N=1$, $\nu_0=\frac{3}{1}$, $V_b(0)=20$). For the case when $\omega_0=120$ the large primary resonance is located at $\bar{k}_a=60$ and the small primary is located at $\bar{k}_b=20$. Thus there are 40 quantum states separating the centers of these two resonances. In Ref. 12, we showed (and our current calculations support the fact) that the largest secondary resonances lie between the two primaries and this is the region we focus on here. We have probed the Hilbert space in the following way. We fix $V_b(0)=20$ and choose values for $V_a(0)$ ranging between 30 and 190. We start all the probability at the center of the small primary. That is, we set $|\Psi_{20}^{(0)}(0)|^2=1$ and $|\Psi_k^{(0)}(0)|^2=0$ for $k\neq 20$ and we integrated Eq. (5.2) for many periods $T=2\pi/\omega_0$ (a time much longer than necessary for the probalility to reach its maximum spread). We then find how probability is spread over states, $\Psi_k^{(0)}(t)$. In Fig. 18, we show the average spread of probability, $\bar{P}_k$, for two cases, $V_a(0)=20$ and $V_a(0)=190$. Note the asymmetry in the spread of probability in the direction of the large primary.

In Fig. 19, we focus on the region $k=30$ to $k=44$ and show the extent of the spread for nine different values of $V_a(0)$ [with $V_b(0)=20$]. The secondary resonance pairs $\nu_1=\frac{4}{3}$ lie at $\bar{k}_0=20$ and $\bar{k}_1=30$. From Fig. 13 we predict overlap to occur when $X(0)=0.23$ and $Y(0)=0.158$. However, for this case, we do not expect the theory to work well. The half-width of the resonance at $\bar{k}_0=20$ is $\Delta k_b\approx[2V_b(0)]^{1/2}=6.3$. Thus the resonance at $\bar{k}_1=30$ lies within three quantum states of it. We expect WKB to give too large a value for $X(0)$. In addition the stable manifold curve is almost flat and is very sensitive to any error in $X(0)$. For example $X(0)=0.23$ we get $V_a(0)=42$ while for $X(0)=0.2$ we get $V_a(0)=30$. At $V_a(0)=30$ we see that overlap has occurred. Probability has spread between the resonance pair $\nu_1=\frac{4}{3}$.

We expect better results for the resonance pair $\nu_1=\frac{5}{4}$ which lies at $\bar{k}_1=30$ and $\bar{k}_2=36$. The stable manifold in Fig. 13 indicates that there is blockage between $k=30$ and $k=36$ until $X(0)\approx 0.4$ or $V_a(0)\approx 128$. In Fig. 19, we see exponential decay into this region until $V_a(0)\approx 90$. When $V_a(0)\approx 110$, the probability has spread into the region between resonance pairs $\nu_1=\frac{5}{4}$ and $\nu_1=\frac{6}{5}$ which, according to Fig. 13, overlap at about the same values of $X(0)$.

There is another interesting phenomenon at work here. We see that the probability for $V_a(0)=130$ is pushed backward relative to where we expect it to be. This appears to be due to the fact that it is hitting the edges of the large resonance that is pushing into that region from the right. In Fig. 20 we show the edge of the large resonance (shaded area), whose position we have established using the estimate for the half-width, $\Delta k_a\approx[2V_a(0)]^{1/2}$. From Ref. 12, this gives fairly good predictions to within a few quantum states. For $V_a(0)=110$ it has not yet reached $k=44$ (rightmost extent of our figure). However, at $V_a(0)=130$ it just begins to enter the figure and at

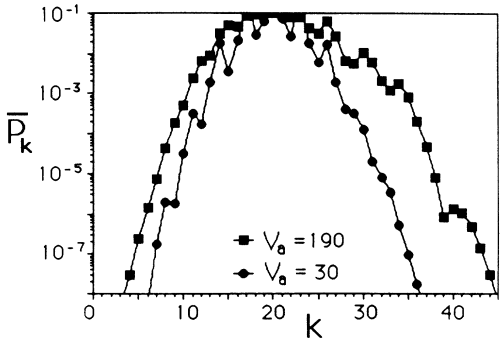

FIG. 18. A plot of $\bar{P}_k$ for $M_a(0)=1$, $M_3(0)=3$, $\omega_0=120$, $V_b(0)=20$, and $V_a(0)=30$ and 190 as indicated in the figure. The same initial conditions were used as in Eq. (6.1). Note that the vertical axis is a log scale.

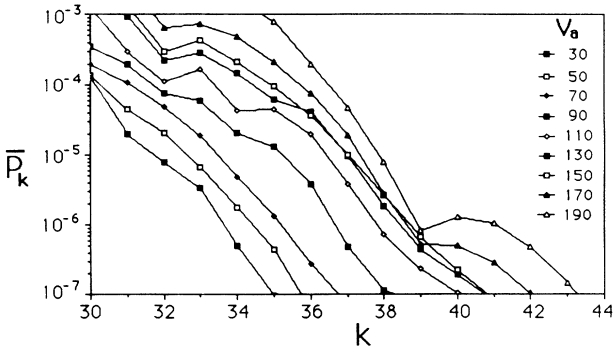

FIG. 19. The average probability, $\bar{P}_k=\frac{1}{10}\sum_{j=1}^{5}[|\Psi_k^{(0)}(2j)|^2+|\Psi_k^{(0)}(2.3j)|^2]$ obtained by solving Eq. (2.3) numerically for $M_a(0)=1$, $M_3(0)=3$, $\omega_0=120$, $V_b(0)=20$, and a variety of values of $V_a(0)$ as indicated in the figure. The initial conditions for all curves are $|\Psi_{20}^{(0)}(0)|^2=1$ and $|\Psi_k^{(0)}(0)|^2=0$ for $k\neq 20$. Note that the vertical axis is a log scale.

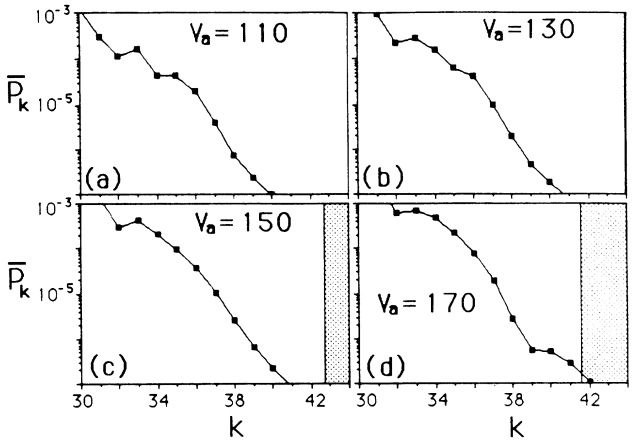

FIG. 20. Plot of curves from Fig. 19 indicating their position relative to the edge of the primary resonance. The large primary has a half-width of $[2V_a(0)]^{1/2}$ and for $\omega_0=120$ is centered at $k=60$. The spread of probability appears to be blocked by the edge of the large primary [cf. (c) and (d)] before it finally penetrates into the interior of the large primary resonance region.

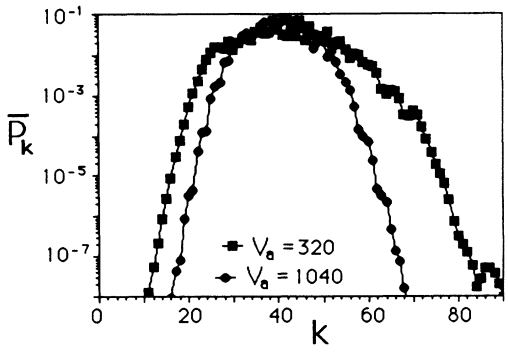

FIG. 21. A plot of $\bar{P}_k$ for $M_a(0)=1$, $M_3(0)=3$, $\omega_0=240$, $V_b(0)=80$, and $V_a(0)=320$ and 1040 as indicated in the figure. The same initial conditions were used as in Eq. (6.1). Note that the vertical axis is a log scale.

$V_a(0)=150$ it has blocked and pushed the probability back from its expected position. When $V_a(0)=170$, the probability has overcome KAM barriers at the edge of the large primary and has penetrated into it. At this point, we can say that overlap between the two primary resonances has occurred. Note that our stable manifolds predict that probability spreads between the two primary resonances for $V_a(0)\approx 130$. We observe it occurring for $150\leq V_a(0)\leq 170$. The Chirikov prediction gives $X(0)+Y(0)=1$ or $X(0)=0.843$ and $V_a(0)=570$ when $V_b(0)=20$. Thus the renormalization predictions are extremely good.

Case II ($\omega_0=240$, $N=1$, $\nu_0=\frac{3}{1}$, $V_b(0)=80$). For this case the large primary resonance is located at $\bar{k}_a=120$ and the small primary is located at $\bar{k}_b=40$ so that 80 quantum states separate the two primaries. We set $V_b(0)=80$ and allow $V_a(0)$ to range between $V_a(0)=320$ and $V_a(0)=1040$. As before, we start all probability at the center of the small primary and let the probability flow to the maximum extent allowed by the KAM barriers. In Fig. 21 we show $\bar{P}_n$ for two limiting cases,

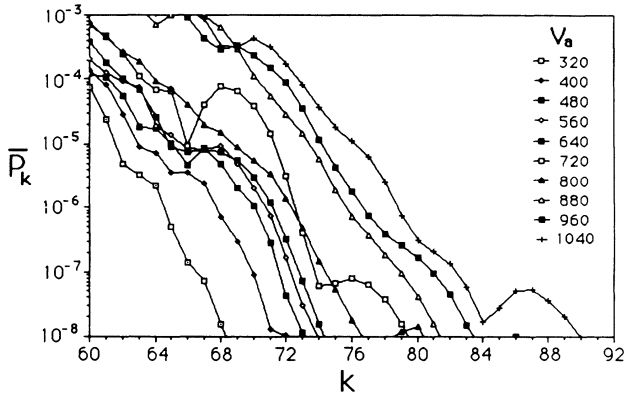

FIG. 22. The average probability, $\bar{P}_k=\frac{1}{10}\sum_{j=1}^{5}[|\Psi_k^{(0)}(2j)|^2+|\Psi_k^{(0)}(2.3j)|^2]$ obtained by solving Eq. (2.3) numerically for $M_a(0)=1$, $M_3(0)=3$, $\omega_0=240$, $V_b(0)=80$, and a variety of values of $V_a(0)$ as indicated in the figure. The initial conditions for all curves are $|\Psi_{40}^{(0)}(0)|^2=1$ and $|\Psi_k^{(0)}(0)|^2=0$ for $k\neq 40$. Note that the vertical axis is a log scale.

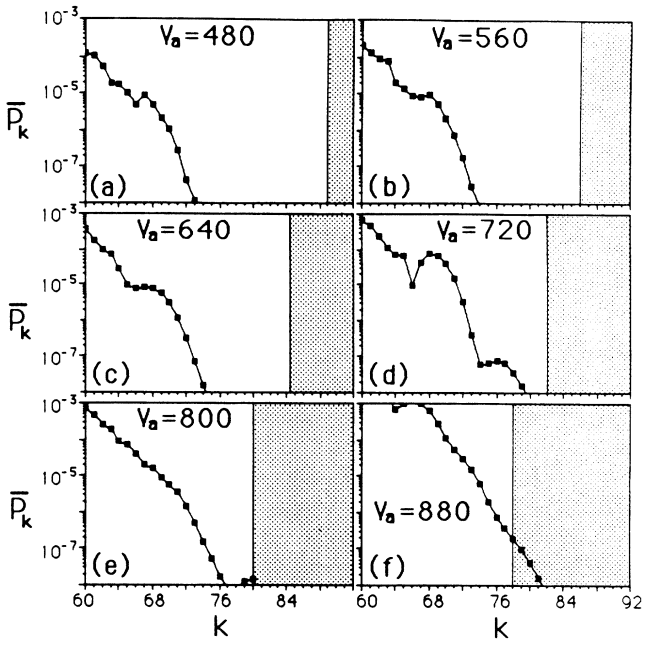

FIG. 23. Plot of curves from Fig. 22 indicating their position relative to the edge of the large primary resonance. The large primary has a half-width of $[2V_a(0)]^{1/2}$ and for $\omega_0=240$ is centered at $k=120$. The spread of probability appears to be blocked by the edge of the large primary [cf. (d) and (e)] before it finally penetrates into the interior of the large primary resonance region.

$V_a(0)=320$ and $V_a(0)=1040$. Again note the asymmetry. In Fig. 22, we show a sequence of values of $\bar{P}_n$ for values of $V_a(0)$ ranging from 320 to 1040. The resonance pair $\nu_1=\frac{4}{3}$ lies at $\bar{k}_0=40$ and $\bar{k}_1=60$. The half-width of the resonance at $\bar{k}_0=40$ is $\Delta k=12.6$ so the secondary lies further away than in the previous case. We predict overlap of this resonance pair at $X(0)=0.23$ or $V_a(0)=170$ [$X(0)=0.2$, $V_a(0)=128$]. So overlap has occurred by $V_a(0)=320$. The secondary resonance pair $\nu_1=\frac{5}{4}$ lies at $\bar{k}_1=60$ and $\bar{k}_2=72$, while secondary resonance pair $\nu_1=\frac{6}{5}$ lies at $\bar{k}_2=72$ and $\bar{k}_3=80$. We predict overlap when $X(0)=0.4$ or $V_a(0)=512$. From Fig. 22, we see that the probability has spread into the regions between resonance pairs $\nu_1=\frac{5}{4}$ and $\nu_1=\frac{6}{5}$ when $V_a(0)=720$. For $V_a(0)=800$ the spread of the probability has stopped. In Fig. 23 we show the position of the large primary (shaded region). For $V_a(0)\geq 880$ the probability has entered the region of the large primary and overlap between two primary resonances had occurred. Chirikov predicts this to happen for $V_a(0)\approx 2700$ while the renormalization predictions give $V_a(0)\approx 720$.

VII. CONCLUSION

In the preceding sections we have developed a renormalization transformation which is based on the existence of higher-order nonlinear resonances in quantum-dynamical systems. It is interesting that the renormalization mapping itself depends on dimensionless

variables and does not depend explicitly on Planck's constant $\hbar$. The mapping relates the wave numbers and amplitudes of the resonance zones on successively smaller scales in the Hilbert space, and gives fairly good predictions for the parameter values at which resonance overlap occurs in the Hilbert space. One might object that the renormalization mapping has no meaning as we go to scales where the resonance pairs have a size smaller than the spacing between quantum numbers. However, in practice, the growth of resonance amplitudes is so rapid as we cross the stable manifold into the unstable region that the stable manifold still appears to give good predictions in the quantum systems we have looked at.

We have not attempted in this paper to study the deviations of the predictions of our renormalization theory for quantum systems from those of classical renormalization theory. It is known from numerical experiments that it requires stronger external fields to remove KAM barriers in quantum systems than in the corresponding classical systems. There have been attempts to explain this based on semiclassical extensions of classical scaling theory.[14-19] Perhaps the simplest is that due to MacKay and Meiss[14,15] who simply require that a Cantorus ceases to be barrier to quantum wave functions when the flux (classical phase-space area) ΔW across the Cantorus satisfies the condition $\Delta W > \hbar$ rather than $\Delta W > 0$ as is true classically. This gives quite good qualitative predictions for the shifts from classical behavior observed in quantum systems.

Understanding when resonance overlap occurs in a given quantum system is important because it leads to extension of the wave function in that region and may have profound effects on the dynamics (such as ionization, if we are considering electron states in a molecule). We see that KAM behavior causes localization of the wave function in Hilbert space. However, this type of localization must be distinguished from Anderson localization[20] which occurs in regions of extreme resonance overlap (where KAM behavior has been destroyed).

It is important to note that *the systems we have considered exhibit highly nonlinear behavior* and in fact show many of the phenomena observed in nonlinear classical systems (except chaos if the spectrum is discrete) *even though the Schrödinger equation for this system is linear.* The type of behavior we have observed here is probably typical of most quantum systems which have two degrees of freedom and nonlinear Hamiltonians even though the Schrödinger equation is linear.

ACKNOWLEDGMENTS

L.E.R. wishes to thank the Institute for Nonlinear Science, University of California, San Diego; the University of Texas University Research Foundation; and the Welch Foundation of Texas, Grant No. F-1051 for partial support of this work. She also thanks M. Mikeska and J. Cornelius for their invaluable help with the I.N.L.S. computer system.

APPENDIX A: QUANTUM STANDARD MAP

In this appendix we write the quantum standard map in terms of the resonance picture. The standard map may be viewed as describing a rotor subject to repeated δ-function kicks occurring with period T and with an amplitude which depends on the angular position of the rotor. The Hamiltonian for the classical standard map can be written

$$H = \frac{J^2}{2I} + K\cos(\theta)\sum_{n=-\infty}^{\infty}\delta(t-nT) \tag{A1}$$

where J is the angular momentum of the rotor, θ is its angular position, and I is its momentum of inertia. The parameter K is the strength of the kicks and T is their period. If we note the identity

$$\sum_{n=-\infty}^{\infty}\delta(t-nT) = \frac{2}{T}\sum_{k=1}^{\infty}\cos\left[\frac{2\pi kt}{T}\right] + \frac{1}{T} \tag{A2}$$

and note that the angular momentum operator can be written $\hat{J} = -i\hbar\partial/\partial\theta$, then the quantum Hamiltonian can be written

$$\hat{H} = -\frac{\hbar^2}{2I}\frac{\partial^2}{\partial\theta^2} + \frac{K}{T}\cos(\theta) + \frac{K}{T}\sum_{k=1}^{\infty}\left[\cos\left[\theta - \frac{2\pi kt}{T}\right] + \cos\left[\theta + \frac{2\pi kt}{T}\right]\right]. \tag{A3}$$

The Schrödinger equation for the δ-kicked rotor, in the angle picture, can be written

$$i\hbar\frac{\partial\Psi}{\partial t} = -\frac{\hbar^2}{2I}\frac{\partial^2\Psi}{\partial\theta^2} + \frac{K}{T}\sum_{k=-\infty}^{\infty}\left[\cos\left[\theta - \frac{2\pi kt}{T}\right]\right]\Psi \tag{A4}$$

where $\Psi = \Psi(\theta, t)$. In terms of the angular momentum quantum number n the Schrödinger equation takes the form

$$i\hbar\frac{\partial\Psi_n}{\partial t} = \frac{\hbar^2 n^2}{2I}\Psi_n + \frac{K}{2T}\sum_{k=-\infty}^{\infty}(e^{-i\omega kt}\Psi_{n-1} + e^{i\omega kt}\Psi_{n+1}). \tag{A5}$$

Equation (A5) can be written in dimensionless form. It becomes

$$i\frac{\partial\Psi_n}{\partial\tau} = n^2\Psi_n + \frac{\epsilon}{2}\sum_{k=-\infty}^{\infty}(e^{-i\omega k\tau}\Psi_{n-1} + e^{+i\omega k\tau}\Psi_{n+1}) \tag{A6}$$

where $\tau = \hbar t/2I$, $\omega_0 = 2I\omega/\hbar$, and $\epsilon = 2KI/\hbar^2 T$. Thus, in terms of dimensionless quantities the primary resonance zones are located, in the Hilbert space of angular momentum states, at $n_k = \omega_0 k/2$ and have a half-width of $\Delta n_k = \sqrt{2\epsilon}$. In terms of the original units we have $n_k = \omega kI/\hbar$ and $\Delta n_k = 2(KI/\hbar^2 T)^{1/2}$. If comparison is made with the paper of Grempel, Prange, and Fishman[20] we find for the parameters used in Fig. 10 of that paper, $n_k = 1.3k$ and $\Delta n_k = 1.5$. Thus they are well within the regime of resonance overlap. This is reflected in the fact that their quasienergy eigenstate is spread over many states of the Hilbert space.

APPENDIX B: DRIVEN SQUARE WELL

Let us consider a particle in an infinite square-well potential [$V(x)=0$ for $0<x<2a$ and $V(x)=\infty$ otherwise] driven by a monochromatic external field. The Hamiltonian may be written

$$\hat{H}=\hat{H}_0-\epsilon(|\hat{x}|-a)\cos(\omega t)\ , \tag{B1}$$

where $\hat{H}_0$ is the Hamiltonian for the unperturbed particle in the infinite square-well potential, ϵ and ω are the external field amplitude and frequency, respectively, $\hat{x}$ is the particle position operator, and t is the time. The absolute value $|\hat{x}|$ appears in Eq. (2.1) because we will expand in traveling-wave states $|n\rangle$ (n is an integer) normalized on the interval $-2a$ to $2a$. In the position representation $\langle x|n\rangle=(1/\sqrt{4a})\exp(in\pi x/2a)$. In the traveling-wave basis, matrix elements of $\hat{H}_0$ are given by

$$\langle n'|\hat{H}_0|n\rangle=\frac{\hbar^2\pi^2n^2}{8ma^2}\delta_{n',n} \tag{B2}$$

where $\hbar$ is Planck's constant and m is the mass of the particle. Matrix elements of $\hat{x}$ are given by

$$\langle n'||x||n\rangle=\begin{cases}\dfrac{4a}{\pi^2(n'-n)^2} & \text{for } (n'-n) \text{ odd}\\ 0 \text{ for } (n'-n) \text{ even}\ .\end{cases} \tag{B3}$$

The total Hamiltonian can be written

$$\hat{H}=\sum_{n=-\infty}^{\infty}\hbar\Omega n^2|n\rangle\langle n| +\frac{4a\epsilon\cos(\omega t)}{\pi^2}\sum_{n=-\infty}^{\infty}\sum_{n'=-\infty}^{\infty}\frac{|n'\rangle\langle n|}{(n'-n)^2} \tag{B4}$$

($n-n'$ odd) where $\Omega=\hbar\pi^2/8ma^2$. It is useful to introduce a change of summation variables, $N=n'+n$ and $M=n'-n$. Then the Hamiltonian can be written

$$\hat{H}=\sum_{n=-\infty}^{\infty}\hbar\Omega n^2|n\rangle\langle n|+\frac{4a\epsilon\cos(\omega t)}{\pi^2} \times\sum_{N=-\infty}^{\infty}\sum_{M=-\infty}^{\infty}\frac{1}{M^2}|\tfrac{1}{2}(N+M)\rangle\langle\tfrac{1}{2}(N-M)| \tag{B5}$$

(M and N odd) and the Schrödinger equation for this system can be written

$$i\hbar\frac{\partial\langle n|\Psi(t)\rangle}{\partial t}=\hbar\Omega n^2\langle n|\Psi(t)\rangle +\frac{4a\epsilon\cos(\omega t)}{\pi^2}\sum_{M=-\infty}^{\infty}\frac{1}{M^2}\langle n-M|\Psi(t)\rangle \tag{B6}$$

(M odd) where $|\Psi(t)\rangle$ is the probability amplitude for the system at time t. Because the potential at the walls of the square well is infinite, the wave function must be zero at the walls. Thus $\langle 0|\Psi(t)\rangle=\langle 2a|\Psi(t)\rangle=0$ and $\langle n|\Psi(t)\rangle=-\langle -n|\Psi(t)\rangle$.

Let us now write the Schrödinger equation in terms of dimensionless quantities. Let $\tau=\Omega t$, $\omega_0=\omega/\Omega$, and $q=2a\epsilon/\hbar\Omega\pi^2$. We then find

$$i\frac{\partial\langle n|\Psi(\tau)\rangle}{\partial\tau}=n^2\langle n|\Psi(\tau)\rangle+q\sum_{M=-\infty\, M\text{ odd}}^{\infty}\frac{1}{M^2}\{[e^{-i\omega_0\tau}\langle n-M|\Psi(\tau)\rangle+e^{i\omega_0\tau}\langle n+M|\Psi(\tau)\rangle]\}\ . \tag{B7}$$

It is also useful to introduce angle variables $\phi=\pi x/2a$. We can transform to the angle picture by means of the transformation $\langle\phi|\Psi(\tau)\rangle=\sum_{n=-\infty}^{\infty}\langle\phi|n\rangle\langle n|\Psi(\tau)\rangle$, where $\langle\phi|n\rangle=e^{in\phi}/\sqrt{2\pi}$. The range of ϕ is $-\pi$ to π. The physical range (in the well) is 0 to π. Then the Schrödinger equation takes the form

$$i\frac{\partial\langle\phi|\Psi(\tau)\rangle}{\partial\tau}=-\frac{\partial^2\langle\phi|\Psi(\tau)\rangle}{\partial\phi^2}+2q\sum_{\substack{M=-\infty\\ M\text{ odd}}}^{\infty}\frac{1}{M^2}[\cos(M\psi-\omega_0\tau)]\langle\phi|\Psi(\tau)\rangle\ . \tag{B8}$$

Equation (B8) describes the behavior of a particle in the presence of an infinite number of traveling cosine potential wells, each traveling with different speed. Each traveling potential well gives rise to a nonlinear primary resonance zone in Hilbert space. In Refs. 8 and 11 it was shown that the primary resonance zone due to cosine potential $\cos(M\phi-\omega_0\tau)$ (where M can be positive or negative) is centered in Hilbert space at quantum number $n_M^{pr}=\omega_0/2M$ and has a half-width given approximately by $\Delta n_M^{pr}=2\sqrt{q/|M|}$.

*Permanent address: Department of Physics, Xuzhou Teacher's College, P.R. of China.

[1]J. Greene, J. Math. Phys. **20**, 1183 (1979).
[2]S. J. Shenker and L. P. Kadanoff, J. Stat. Phys. **27**, 631 (1982).
[3]R. S. MacKay, Physica **7D**, 283 (1983).
[4]D. F. Escande and F. Doveil, J. Stat. Phys. **26**, 257 (1981); Phys. Lett. **83A**, 307 (1981); Phys. Scr. **T2**, 126 (1982); D. F. Escande, Phys. Rep. **121**, 165 (1985).
[5]L. E. Reichl and W. M. Zheng, in *Directions in Chaos*, edited by Hao Bai-lin (World Scientific, Singapore, 1987), Vol. I.
[6]T. Geisel, G. Radons, and J. Rubner, Phys. Rev. Lett. **57**, 2883 (1986).

[7]R. C. Brown and R. E. Wyatt, Phys. Rev. Lett. **57**, 1 (1986).
[8]G. P. Berman and G. M. Zaslavsky, Phys. Lett. **61A**, 295 (1977); G. P. Berman, G. M. Zaslavsky, and A. R. Kolovsky, *ibid.* **87A**, 152 (1982); G. P. Berman and A. R. Kolovsky, *ibid.* **95A**, 15 (1983); G. P. Berman, G. M. Zaslavsky, and A. R. Kolovsky, Zh. Eksp. Teor. Fiz. **81**, 506 (1981) [Sov. Phys.—JETP **54**, 272 (1981)].
[9]L. E. Reichl and W. A. Lin, Phys. Rev. A **33**, 3598 (1986).
[10]W. A. Lin and L. E. Reichl, Phys. Rev. A **36**, 5099 (1987); **37**, 3972 (1988); **40**, 1055 (1989).
[11]M. Toda and K. Ikeda, J. Phys. A **20**, 3833 (1987).
[12]L. E. Reichl, Phys. Rev. A **39**, 4817 (1989).
[13]G. P. Berman and A. R. Kolovsky, Phys. Lett. A **125**, 188 (1987).
[14]R. S. MacKay and J. D. Meiss, Phys. Rev. A **37**, 4702 (1988).
[15]J. D. Meiss, Phys. Rev. Lett. **62**, 1576 (1989).
[16]D. R. Grempel, S. Fishman, and R. E. Prange, Phys. Rev. Lett. **53**, 1212 (1984).
[17]S. Fishman, D. R. Grempel, and R. E. Prange, Phys. Rev. A **36**, 289 (1987).
[18]G. Radons and R. E. Prange, Phys. Rev. Lett. **61**, 1691 (1988).
[19]R. V. Jensen, S. M. Susskind, and M. M. Sanders, Phys. Rev. Lett. **62**, 1472 (1989).
[20]D. R. Grempel, R. E. Prange, and S. Fishman, Phys. Rev. A **29**, 1639 (1984).

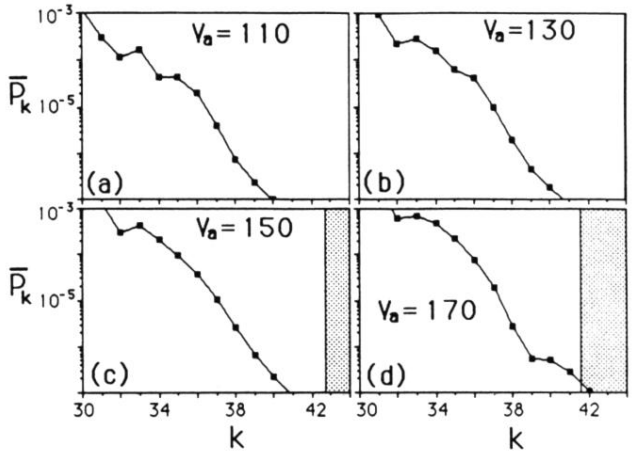

FIG. 20. Plot of curves from Fig. 19 indicating their position relative to the edge of the primary resonance. The large primary has a half-width of $[2V_a(0)]^{1/2}$ and for $\omega_0 = 120$ is centered at $k = 60$. The spread of probability appears to be blocked by the edge of the large primary [cf. (c) and (d)] before it finally penetrates into the interior of the large primary resonance region.

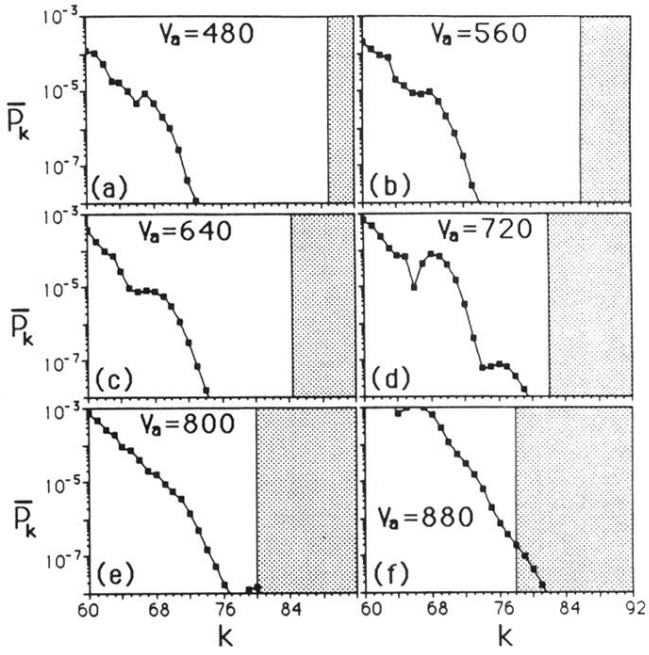

FIG. 23. Plot of curves from Fig. 22 indicating their position relative to the edge of the large primary resonance. The large primary has a half-width of $[2V_a(0)]^{1/2}$ and for $\omega_0=240$ is centered at $k=120$. The spread of probability appears to be blocked by the edge of the large primary [cf. (d) and (e)] before it finally penetrates into the interior of the large primary resonance region.